Title: Anatomical basis and physiological role of cerebrospinal fluid transport through the murine cribriform plate

Authors: Jordan N. Norwood[1], Qingguang Zhang[2], David Card[3], Amanda Craine[4], Timothy M. Ryan[5], Patrick J. Drew[2,4,6]

Affiliations:

[1]Cellular and Developmental Biology Graduate Program, Pennsylvania State University, University Park, PA 16802
[2]Department of Engineering Science and Mechanics, Pennsylvania State University, University Park, PA 16802
[3]Department of Physics, Pennsylvania State University, University Park, PA 16802
[4]Department of Biomedical Engineering, Pennsylvania State University, University Park, PA 16802
[5]Department of Anthropology, Pennsylvania State University, University Park, PA 16802
[6]Department of Neurosurgery, Pennsylvania State University, University Park, PA 16802

Abstract: Cerebrospinal fluid (CSF) flows through the brain, transporting chemical signals and removing waste. CSF production in the brain is balanced by a constant outflow of CSF, the anatomical basis of which is poorly understood. Here we characterized the anatomy and physiological function of the CSF outflow pathway along the olfactory sensory nerves through the cribriform plate, and into the nasal epithelia. Chemical ablation of olfactory sensory nerves greatly reduced outflow of CSF through the cribriform plate. The reduction in CSF outflow did not cause an increase in intracranial pressure (ICP), consistent with an alteration in the pattern of CSF drainage or production. Our results suggest that damage to olfactory sensory neurons (such as from air pollution) could contribute to altered CSF turnover and flow, providing a potential mechanism for neurological diseases.

Figures: 10
Supplemental Figures: 5
Pages: 38
Tables: 3
Abstract: 131 words
Introduction: 503 words
Main Text: 4,783 words

Correspondence to: Patrick J Drew, pjd17@psu.edu
Department of Engineering Science & Mechanics
W-317 Millennium Science Complex
Pennsylvania State University
University Park, PA 16802
or
Jordan N. Norwood, jnn120@psu.edu
W-326 Millennium Science Complex
Pennsylvania State University
University Park, PA 16802

The brain has a very high metabolic rate, but lacks a conventional lymphatic system for clearance of metabolites and waste products. It is thought that the movement of cerebrospinal fluid (CSF) plays an important role in removing these waste products[1]. CSF is constantly produced by the choroid plexus[2], circulates through the subarachnoid space and into the brain via a periarterial route[3], and then exits the brain via several routes[4–7]. Normal aging is accompanied by decreases in CSF production and increases in CSF outflow resistance[8–10]. CSF turnover is disrupted in pathological conditions such as Alzheimer's disease (AD) and normal pressure hydrocephalus (NPH)[11–13]. The balance between CSF production and outflow plays a key role in setting and maintaining the intracranial pressure (ICP)[14]. Because CSF production is actively regulated to maintain normal ICP[15], damage to the outflow pathways could drive compensatory decreases in CSF production and turnover[10]. This lowered production and turnover of CSF will result in decreased waste clearance, as is seen in aging and some neurological diseases.

While there are lymphatic vessels in the meninges[16,17], there is evidence in both humans and other mammals pointing to drainage of the CSF through the cribriform plate (CP)[6,9,18–27]. The CP is a fenestrated bony plate of the ethmoid bone that separates the cranial and nasal cavities. Once through the plate, CSF is absorbed by lymphatic vessels in the nasal mucosa and drained into the cervical lymph nodes[28]. There has been speculation that interstitial fluid (ISF) and CSF leave the brain via the extracellular space between olfactory sensory nerve (OSN) axon bundles[29], as the intercellular space between axon bundles provide low-resistance directed pathways for fluid flow[30]. Acute blockage of CSF outflow by surgically obstructing the CP results in an increase in resting ICP[31] and outflow resistance[32], providing evidence for a drainage role of the trans-cribriform plate pathway. Intriguingly, there may be a connection between the patency of the clearance pathway through the CP and neurodegenerative diseases[9,33]. However, visualization of CSF flow through this structure is challenging. The neurons whose axons make up the nerve bundles that traverse the CP, OSNs, are exposed to environmental toxins (such as air pollutants[34]), which epidemiological studies have associated exposure to neurodegenerative diseases. Furthermore, anosmia and decreased acuity in the sense of smell, which will result from OSN damage, reliably precede many neurological disorders[34]. Thus, damage to or decreases in the numbers of the OSN axons could increase the resistance to CSF outflow, triggering a downregulation in CSF production and turnover. However, a method to maintain the three-dimensional structure of the hard, calcified plate and traversing axons and soft tissues to visualize the microscopic anatomical basis of this movement has been lacking. To better understand the role of the CP CSF outflow pathway, we characterized the cellular anatomy of the structures that traverse the CP and explored the chronic effects of OSN ablation on CSF turnover. We also found that OSN ablation disrupted CSF drainage through the CP, but normal ICP was maintained by a reduction in CSF production.

Results

Macroscopic structure of the cribriform plate

We first examined the macroscopic anatomical structure of the mouse CP to elucidate any stereotyped anatomical structure of the calcified tissue. While the anatomy of the CP has been studied in humans[35] and other large mammals, both extinct and extant[36–39], the structure of the mouse CP has not been as well characterized. To visualize the 3-D anatomy of the calcified bone of the CP, skulls of adult mice (3 Swiss Webster and 3 C57BL/6J) were de-fleshed by dermestid beetles, and imaged with micro-CT. Reconstructed CT images from an example mouse are shown in Fig. 1A-C, showing the typical morphology of the murine CP. Photographs of the CP after removing the caudal portion of the skull showed similar structure (Fig. 1D). The side of the plate adjacent to the olfactory bulb was not planar, but rather convex to accommodate the rounded shape of the anterior ventral face of the olfactory bulbs (Fig. 1E); consequently, thin sections (like those obtained using traditional histology) will only contain a fraction of the structure. We observed a calcified ridge along the midline of the CP (crista galli) with an irregular perforation pattern, with many small (<200μm diameter) foramina (holes). While the positioning, number, and size of the smaller foramina were variable across mice, there were four major foramen appearing in the same locations in all mice imaged. Bilateral foramina were located on the anterior aspect of the plate, lateral to the crista galli, and midway along the dorsal ventral axis of the CP on each side (Fig. 1C, D, F). Their location and structure were consistent across all animals examined with micro-CT. To quantify the total area of all the foramina (see methods), maximum intensity projections were made along the axis perpendicular to the face of the plate (Fig. 1F). We found the total area of the foramina was 1.88±0.29mm^2 (mean±std, n=6, pooling both C57BL/6J and Swiss Webster mice) and the total area of the plate was 9.76±1.12mm^2 (mean±std, n=6, pooling both C57BL/6J and Swiss

Webster mice), similar to previous reports[39]. CT images with C57BL/6J and Swiss Webster mice showed similar CP morphology (Supplementary Figure 1A-D), suggesting that for these two strains, there are minimal strain differences. While a significant difference in total plate area (Fig. 1G) was observed between C57BL/6J ($10.693\pm0.374mm^2$) and Swiss Webster mice ($8.821\pm0.607mm^2$), no significant difference was observed for total foramina area (Fig. 1G) or in the ratio of foramina area to plate area (Fig. 1H). Because the bone is impermeable to fluid movement, these holes will be the only outlet for CSF and ISF flow through the CP, and the nature of the soft tissue filling them (olfactory nerves, blood vessels, or lymphatic vessels) will play an important role in directing the flow of CSF and ISF.

Olfactory nerves enter through the primary foramina

We then asked which foramina in the CP were traversed by OSN axons. However, the junction of the olfactory bulb and nerves is difficult to visualize histologically since the calcified CP, which the OSNs pass through, is immediately adjacent to the soft brain. To maintain the spatial alignment between the soft tissue and CP during sectioning, the bones of the skull must first be softened by decalcification. Traditional decalcification techniques require soaking the tissue in EDTA for several weeks[40,41], which results in degradation of epitopes, making it incompatible with immunohistochemistry. We developed a rapid decalcification protocol using formic acid (see Methods), allowing us to decalcify the skull within two days, thereby preserving epitopes for immunohistochemical labeling. Using formic acid decalcification, we were able to section the skull in a way that maintained the pathway of the OSNs (labeled with an anti-olfactory marker protein (OMP) antibody[42,43]) traversing the CP (Fig. 1L-M). OMP-expressing OSN axon bundles were observed traversing the CP and synapsing onto the olfactory bulb (Fig. 1L, M), with two major axon bundles (yellow arrows) on the left and right sides (Fig. 1L). These OSN axon bundles filled the four major foramen observed in the CP (Fig. 1C, D, F). In the coronal plane, smaller axon bundles traversed the CP through the smaller foramina bordering the crista galli (Fig. 1M). These results show that there are two distinct types of foramen in the CP: the major foramen, through which the larger OSN bundles pass through, and a multitude of smaller holes whose position varied across animals and some of which carried smaller OSN bundles. Because extracellular fluid flow preferentially moves parallel to axon tracts[30], these nerves can provide directed conduits for ISF and CSF to move from the cranial cavity into the nasal cavity.

Blood vessels traverse the cribriform plate

We then asked what other soft tissues were contained within the small foramen, as the nature of these tissues will influence the flow of fluid out of the cranial compartment. The presence of blood and lymphatic vessels in the foramina were assessed because both tissue types could be conduits for fluid flow[3,16,17].

We first looked at whether blood vessels traversed the CP by either filling the vessel lumen with FITC-albumin[44], or labeling the endothelial cells by perfusing the vasculature with the fluorescent lipophilic dye DiI[45]. FITC-Albumin filled vessels were found to run parallel to the OSNs traversing the CP (Fig. 2D-E). Blood vessels, labeled by DiI, were also clearly visible in the smaller foramina (Fig. 2M-O). Both olfactory nerve bundles and blood vessels were present in other foramina (Fig. 2M). These results show that blood vessels traverse the CP in the mouse, much like the ethmoidal arteries observed in humans[46–48], linking the vascular territories of the nasal epithelia and brain.

Aquaporins at the olfactory nerve-bulb interface

Aquaporins (AQP) greatly enhance the permeability of cells to water[49], and their presence would help facilitate the movement of fluid down the pressure gradient. The different aquaporin protein subtypes have similar structure, but differ in their localization throughout the body[49]. We used immunofluorescence to examine the expression of aquaporin channels at the interface between the CP and olfactory bulbs. We validated each antibody using mouse kidney tissue (Supplementary Figure 2J-K)[50–52]. We first looked at the expression of aquaporin-1 (AQP1), as previous work has shown that AQP1 is expressed along the periphery of the olfactory bulb in neonatal mice[53], and there is a high level of expression of AQP1, 3, and 5, within the nasal cavity[54]. The junction of the olfactory bulb and nerve is a prime exit route for CSF and ISF into the nasal cavity. Expression of aquaporins in this area would facilitate the flow of fluid out of the olfactory bulb and subarachnoid space, into the nasal cavity (via OSNs). We observed high levels of AQP1 expression on the olfactory nerve layer, down to the glomeruli, and in the lamina propria of the neuroepithelium at both the medial (Fig. 2F-G) and dorsal (Fig. 2H-K) junctions of the olfactory bulb and nerve. AQP1 was also observed lining the foramina of the CP along the crista galli (Fig. 2L, N-O). High levels of AQP1 expression were not seen in any other brain area, with the exception of the choroid plexus (data not shown), strongly suggesting the interface between the olfactory nerve and bulb is a brain region with a high fluid flux flowing through it.

We then examined the expression of AQP4, which is enriched around astrocyte endfeet in the cortex[55] and is hypothesized to play a role in transport of fluid through the glymphatic system[3] (though this is controversial[56]). We observed low levels of expression of AQP4 within the olfactory nerve and neuroepithelium (Supplementary Figure 2F-G). The localization of other aquaporins, AQP2, AQP3, and AQP5, were also examined at the olfactory bulb and nerve junction, but their expression was limited to the neuroepithelium (Supplementary Figure 2D-E, H-I). The highly enriched expression of aquaporins observed in the tissues at the junctional area of the olfactory nerve and bulb could provide a low-resistance pathway for ISF to pass from the olfactory bulb to the olfactory nerves, out of the cranium, and ultimately into the nasal cavity.

Lymphatic vessels traverse the cribriform plate

Lymphatic vessels play a role in moving ISF throughout the body and are found in the meninges[16,17] and nasal epithelium[27]. Lymphatic vessels crossing the CP could play a role in transporting fluid from the cranial cavity to the nasal cavity. We used LYVE1-GFP (lymphatic vessel endothelial hyaluronan receptor 1) or LYVE1-tdTomato mice (see Methods) to visualize lymphatic vessels. To verify that the LYVE1-GFP or LYVE1-tdTomato transgene was not expressed in vascular endothelial cells, the mice were perfused using either DiI or FITC-albumin, respectively, and the cervical lymph nodes were examined to detect cross-labeling (Supplementary Figure 3A-B). Expression of *LYVE1* was observed in the meningial lymphatics, while minimal cross-labeling with fluorescent dye conjugated to phalloidin (which will preferentially label F-actin of arteries[57]) was observed (Supplementary Figure 3C-D). Surprisingly, we observed blood vessel (identified by FITC-albumin fills) endothelial cells that expressed *LYVE1* throughout the brain (Supplementary Figure 3F-G). We also observed non-lymphatic cells of an unknown type in the frontal cortex expressing *LYVE1* (Supplementary Figure 3H-I) that were GFAP, NeuN, Oligo1, and CD164 negative (Supplementary Figure 3J-U), but were occasionally MRC1 (mannose receptor 1) positive (Supplementary Figure 3R-S). Interestingly, we found a few LYVE1$^+$ vessels (both DiI and FITC-albumin negative) adjacent to OSNs in the nasal cavity (Fig. 3D-G), lining holes in the lamina propria of the neuroepithelium, and traversing the CP (Fig. 3H-K). Although *LYVE1* is not expressed exclusively in lymphatic vessels, these results demonstrate that LYVE1$^+$ lymphatic vessels traverse the CP and could facilitate the movement of fluid from the brain compartment to the nasal compartment.

Visualization of CSF flow through the cribriform plate

To visualize CSF flow in the regions downstream from the cisterna magna, we injected the high-contrast Evans blue (EB)[58–61] dye into the cisterna magna (Fig. 4A). When injected into the blood stream, EB binds to albumin in the plasma making it a high molecular weight tracer. However, protein concentrations are vastly lower in the CSF[62], so EB will be unattached to proteins and function as a low molecular weight tracer, freely transported by fluid convection. Injected heads were then decalcified and cut along the midline for imaging as described above (Fig. 4B, D). EB was not observed within the sagittal sinus or the parenchyma, consistent with EB not crossing the glia limitans. Dye was restricted to the subarachnoid space around the brain and spinal column (Fig. 4B-C) and was also clearly visible in the nasal epithelium and the deep cervical lymph nodes (Fig. 4E). To quantify dye movement down the spinal columns, spinal columns were decalcified and cleared using SeeDB[63,64] (Fig. 4C). Cardiac perfusion had no qualitative effect on EB movement, as EB was present in the nasal epithelia even without perfusion (not shown). The observed pathways of CSF (EB dye) flow and drainage through the CP, into the deep cervical lymph nodes, and along the spinal column, are consistent with previous work using radiolabeled tracers, latex fills, and other tracers[20,27,65–67]. We also injected 3kDa-FITCDextran into the cisterna magna to visualize CSF flow and drainage (Fig. 5B-C). To determine the role of LYVE1$^+$ vessels in CSF clearance in the nasal cavity, LYVE1-tdTomato (Ai14) mice were injected with 3kDa-FITCDextran in the cisterna magna (Fig. 5D-I). 3kDa-FITCDextran was observed draining into the nasal cavity along the olfactory nerve (Fig. 5D-F), and co-localizing with LYVE1$^+$ vessels along the olfactory nerve (Fig. 5G-I). These results show that CSF exits the cranial cavity through the CP and is absorbed by nasal LYVE1$^+$ putatively lymphatic vessels.

Chemical ablation of olfactory sensory nerves

We then asked if ablation of OSNs, which removes the low-resistance pathway for fluid flow through the CP, might also block movement of CSF through the CP. Previous work has shown that intranasal treatment of $ZnSO_4$ causes the rapid death of OSNs, and persists for months[68–70]. To chemically ablate OSNs, mice were briefly anaesthetized with isoflurane, and an intranasal solution of $ZnSO_4$ (10% in sterile H_2O) or vehicle (sterile H_2O) was administered to the left nare. Because a loss of the olfactory nerve layer and overall reduction in the size of the olfactory bulb indicates successful ablation of OSNs by $ZnSO_4$[68], we measured the size of the olfactory bulb 2, 10, and 30 days after zinc treatment. A significant decrease in olfactory bulb area was observed compared to vehicle controls 10 days ($t(12) = 6.46$, $p \leq 0.001$, $n = 14$ (7 each group), ttest2) and 30 days ($t(12) = 6.712$, $p \leq 0.001$, $n = 7$ for each group, ttest2) after treatment (Supplementary Figure 4A). Mice treated with $ZnSO_4$ exhibited weight loss initially after treatment, but then began gaining weight at a normal rate starting one week later (Fig. 6A). Running wheels (Med Associates Inc.) were placed in the cages of individually-housed mice (Fig. 6B) to quantify activity levels before and after treatment. $ZnSO_4$ treatment had minimal effects on running behavior (Fig. 6C-D), compared to vehicle controls. These results show that chemical ablation of OSNs with $ZnSO_4$ had minimal effects on the overall health and behavior of the mice.

The olfactory marker protein (OMP) antibody was utilized to histologically examine OSN damage (Fig. 6F-I). Two days after $ZnSO_4$ treatment (Fig. 6G), we observed the beginnings of degeneration of the olfactory nerves. Ten days after $ZnSO_4$ treatment (Fig. 6H), we observed a profound loss of OSN axons, and 30 days after treatment, a complete loss of OSNs traversing the CP from the nasal epithelium was observed (Fig. 6I). We quantified the OMP fluorescent signal intensity between the $ZnSO_4$ treated and vehicle controls (Fig. 6N, Supplementary Figure 4B). A significant decrease in OMP signal was observed in the treated animals compared to the vehicle controls ($F(3, 32) = 259.5$, $p \leq 0.001$, $n = 14$ for vehicle, $n = 5$ for 2 day, $n = 8$ for 10 day, and $n = 9$ for 30 day, one-way ANOVA). These results show that OSNs have largely degenerated 10 days after treatment and are absent a month after intranasal $ZnSO_4$ treatment. As a check for any strain-dependent differences, $ZnSO_4$ treatment was also performed in C57BL/6J mice. Both C57BL/6J and Swiss Webster mice were treated with $ZnSO_4$ (or vehicle control) and histologically examined using Nissl-thionin staining 30 days after treatment (Supplementary Figure 4C-F), showing similar effects.

We then asked if nasal lymphatic vessels were damaged by the $ZnSO_4$ treatment. If lymphatic vessels are a conduit for fluid flow, then damage by $ZnSO_4$ would impede outflow. To detect any changes in lymphatic vessel number or morphology, we histologically examined LYVE1-GFP (Ai6) mice 2, 10, and 30 days after treatment, compared to vehicle controls (Fig. 5J-M). We found no significant change in *LYVE1* expression or localization 2 days after $ZnSO_4$ treatment in LYVE1-GFP mice (Fig. 5K), however, a change in localization at 10 and 30 days after treatment was observed (Fig. 5L-M). These results show that $ZnSO_4$ treatment ablates OSNs while not affecting neighboring lymphatic vessel density in the CP area.

Ablation of OSNs decreases CSF outflow

Because the space between the OSN axons provides a conduit for the outflow of CSF and ISF, removing these axons should decrease outflow of CSF. To visualize any disruption of CSF drainage through the CP after OSN ablation, we injected EB into the cisterna magna (Fig. 7A, C, D, and Supplementary Figure 5A) of mice treated with $ZnSO_4$ and vehicle controls (Fig. 7B). We quantified the average intensity of EB along the rostral-caudal axis within a region of interest (ROI) that encompassed the olfactory bulb and nasal epithelia (see Methods) (Fig. 7B-H). Decreased flow of CSF through the CP would appear as a caudal-shift (leftward-shift) in the dye intensity curve. We plotted the average intensity of dye along the rostral-caudal axis for vehicle and $ZnSO_4$ treated animals, for both the ipsilateral (Fig. 7H, Supplementary Figure 5B-E) and the contralateral (Supplementary Figure 5F-J) sides of treatment. We quantified dye movement using the center of mass along the anterior-posterior axis (Fig. 7I and Supplementary Figure 5K), the peak location along the anterior-posterior axis (Fig. 7J and Supplementary Figure 5L), and the peak value (Fig. 7K and Supplementary Figure 5M) of the dye intensity. We found that 10 and 30 days after treatment, the peak location and center of mass of the dye curve was shifted caudally in $ZnSO_4$-treated mice, relative to vehicle controls, indicating that CSF outflow through the CP was decreased by OSN ablation. For the side ipsilateral to treatment, we saw significant interactions between the effects of time after treatment and the treatment type ($ZnSO_4$ or vehicle) on the center of mass location (Supplementary Table 1). We also saw significant effects on the center of mass and the anterior-posterior peak location by both the duration of treatment and the type of treatment (Supplementary Table 1). Next, to compare the amount of EB collected in the deep cervical lymph nodes after a cisterna magna injection between zinc and vehicle treated mice, the volume of EB injected (2 μL to 4.5 μL) and subsequently the duration of infusion was increased to 45 minutes. No difference in EB collected in the deep cervical lymph nodes was observed between vehicle (Fig. 8B) and zinc treated (Fig. 8C) mice 30 days after treatment. Interestingly, the decrease in CSF outflow through the cribriform plate in zinc treated mice, compared to vehicle mice, was still observed thirty 30 days after treatment (fig. 8D-E), despite the increases in infusion volume and duration. While a significant caudal shift was observed in the center of mass of the EB dye peak, no difference was observed in the dye peak location (Fig. 8F-G) or the distance dye traveled along the spinal column (Fig. 8H). To confirm that this decrease of outflow was not due to some unique aspect of EB, we repeated these experiments by injecting 3kDa-FITCDextran into the cisterna magna. A significant decrease in outflow of 3kDa-FITCDextran into the nasal cavity in $ZnSO_4$-treated mice, relative to vehicle controls, was also observed (Fig. 9). Thus, ablating OSNs blocks CSF outflow through the CP, and this blockage persists for a least a month.

OSN ablation does not affect ICP

The production and outflow of CSF is dynamically balanced[15] in such a way that an increase in outflow resistance will drive a rise in intracranial pressure (ICP)[14,71], unless there is a compensatory reduction of CSF production. To test if the disruption of the nasal CSF outflow pathway causes a rise in ICP, we measured the ICP from awake, head-fixed mice[72,73]. We implanted a titanium headbar and habituated the mice to head fixation on a spherical treadmill[74], allowing them to voluntarily locomote. Locomotion is a natural behavior that causes vasodilation across the cortex[75], which will increase ICP[76]. As a positive control, we also measured ICP in mice with cisterna magna injection of aCSF or kaolin (Fig. 10A). Injections of kaolin into the cisterna magna are known to produce elevations in ICP, and are used to generate an animal model of hydrocephalus[77]. After mice were habituated to head fixation, kaolin or aCSF cisterna magna injections were performed. For ICP measurements, a small craniotomy was performed under isoflurane anesthesia and an ICP sensor (Millar SPR-1000) was placed ~1mm into the cortex. Mice were allowed to wake up from anesthesia on a spherical treadmill, where ICP and treadmill motion were recorded. Data collection started at least 1 hour after the cessation of anesthesia to avoid the effects of anesthetics on ICP and other physiological processes[72,73,78]. We then measured ICP in mice intranasally treated with vehicle or $ZnSO_4$, utilizing the same procedure for measuring ICP of the aCSF and kaolin injected mice (Fig. 10A).

We found that two days after kaolin injections into the cisterna magna ICP significantly increased during locomotion (Supplementary Table 2) compared to aCSF controls (Fig. 10B-C), but not during rest. No statistically significant difference was observed in $ZnSO_4$ treated mice at rest or during locomotion as compared to the vehicle controls (Fig. 10B-C) measured 10, 30, and 60 days after treatment (Supplementary Table 2, 3). Despite the blockage of the nasal CSF outflow pathway, ICP did not increase. This suggests that an alternate outflow route is taken and/or CSF production is decreased

Decreased CSF movement down the spinal column following OSN ablation

A block in CSF drainage accompanied by no change in ICP implies either a compensatory *decrease* in CSF production or an increase in outflow along other pathways, such as the spinal column. To distinguish between these two hypotheses, we examined the spinal columns after a cisterna magna injection of EB into mice treated with intranasal $ZnSO_4$ or vehicle. Since the cisterna magna is 'upstream' from all outflow pathways, including the spinal column, if there is a compensatory increase in the outflow of CSF via the spinal pathway, we would expect dye injected into the cisterna magna to move further down the spinal columns of mice with olfactory nerve ablations as compared to vehicle controls. Conversely, if the CSF production is *reduced* to compensate for the loss of the nasal CSF outflow pathway, we would expect to see a reduction in dye movement down the spinal columns. To differentiate these two possibilities, we extracted the spinal columns and cleared them using SeeDB[63,64] after EB cisterna magna injections. We quantified the distance the dye traveled along the dorsal side of the spinal column for both vehicle and $ZnSO_4$ treated animals, 2, 10, and 30 days after treatment (Fig. 10D-F). While no significant difference between the vehicle and $ZnSO_4$ treatment groups in the distance of dye traveled 2 days after treatment was observed, a significant decrease in the distance traveled was observed for both 10 and 30 days after treatment (Fig. 10G). Our results show that in response to the disruption of the nasal outflow pathway, CSF production was decreased, preventing an elevation in ICP.

Discussion

Utilizing histology, microCT imaging, physiology, and tracer dye injections, we investigated the anatomical basis of CSF outflow through the CP into the nasal cavity. The foramina will permit the flow of fluid out of the brain through the intercellular space between OSN axons, blood vessels, and LYVE1$^+$ vessels traversing through them. We found that aquaporin-1 (AQP1) was localized to the olfactory bulb and nerve junction and lining the foramina of the CP, instead of aquaporin-4 (AQP4), which is the dominant water channel in the CNS[79]. We disrupted CSF drainage through the CP (as well as along the spinal column) by ablating the OSNs. Interestingly, instead of a rise in ICP as expected due to a blockage of CSF drainage, our results are consistent with a reduction in CSF production to maintain a normal ICP. CSF production is not a passive process, but rather one under active neural control[80–82]. As ICP needs to be maintained within a healthy range, there are likely homeostatic processes that sense ICP, and cause compensatory increases or decreases in CSF production, similar to other mechanosensory processes in other organs of the body[83,84]. A potential mechanism mediating this feedback is mechanically-sensitive ASIC3 channels, which are expressed in the ventricles[85], and are sensitive to changes in pressure that are physiologically relevant to ICP regulation. Pathological elevations of ICP due to trauma produce a rise in systemic blood pressure and a decrease in heart rate, known as the Cushing response[86,87], showing the brain has a way of sensing ICP[86], and pressure-sensitive brain regions mediating these responses have been identified[86,87]. A similar response may be occurring in the choroid plexus to compensate for the decreased CSF drainage we observe after $ZnSO_4$ treatment, thus, avoiding the rise in ICP that is normally associated with a decrease in CSF drainage[80,81].

Our dye injections were done under anesthesia and the CSF drainage observed may differ in the awake animal. Although these limitations should be considered, since we observed a difference in drainage between the $ZnSO_4$ and vehicle treated mice, this should still be considered a significant decrease in CSF drainage due to OSN ablation. Although our lymphatic mouse model (Lyve1.Cre.GFP mice crossed with Ai6 or Ai14 reporter lines) exhibited some non-lymphatic specific *LYVE1* expression in vascular endothelial cells in the brain, there were also LYVE1$^+$ vessels along the olfactory nerve that did not co-label with vascular perfusion markers (FITC-albumin fills or DiI staining) and that absorbed dye injected into the cisterna magna. These vessels are putatively lymphatic vessels that transport CSF out of the cranial cavity. Previous work has shown that there is transport of fluid across the CP[20] and acute blockage of the plate (by sealing it with cyanoacrylate glue) blocks transport of radiolabeled albumin[88] establishing the CP as a route of ISF drainage, which then drains into the nasal lymphatics[18,19,21,24,25,33,66,89–94]. Our work elucidates the anatomical basis of CSF transport through the CP and its role in CSF turnover, and demonstrates that damage to the olfactory sensory nerves can impair this pathway.

This work provides a possible mechanism for the observed correlations between neurodegeneration, anosmia, and environmental toxins like air pollution. Although olfactory impairment, or anosmia, occurs during normal aging[95,96], anosmia frequently precedes many neurological disorders[97–101]. Furthermore, studies have shown correlations with the levels of air pollution with olfactory impairment[34,102–105] and neurodegenerative disease pathology, such as Alzheimer's disease[106–111], though the mechanism behind these correlations is unclear. Anosmia has many causes, such as smoking and head trauma[102], and toxin exposure is another source of olfactory deficits. The OSNs are exposed to environmental toxins (such as air pollutants[34]) in the nasal cavity, causing an increased rate of OSN death. A decrease in the number of OSNs may be increasing the resistance to CSF outflow, triggering a downregulation in CSF production to maintain normal ICP. Reduced CSF turnover may be a contributing factor to the buildup of toxic metabolites and proteins that cause neurodegenerative disorders.

Methods

The protocols used in this study were approved by the Institutional Animal Care and Use Committee (IACUC) at the Pennsylvania State University. Mice were maintained on a 12-hour light-dark cycle with ad libitum access to food and water. We used both male and female Swiss Webster (Charles River), C57BL/6J (Jackson Laboratory), and LYVE1-GFP or LYVE1-tdtomato mice. We used a total of 294 mice [60-120 days/29.0±5.8 g]. Partitioning was: Male/female (137/157), Swiss Webster (239), C57BL/6J (9) and LYVE1 mice (52). All anatomy studies were repeated in at least 3 mice. Mice used were ages 60-90 days (young adult). "LYVE1-GFP" mice are the heterozygous offspring of Lyve-1.Cre.GFP$^{+/+}$ (Jackson Laboratory - Stock No: 012601) and Ai6 (RCL-ZsGreen)$^{+/+}$ (Jackson Laboratory - Stock No: 007906) mice. "LYVE1-tdtomato" mice are the heterozygous offspring of Lyve-1.Cre.GFP$^{+/+}$ (Jackson Laboratory - Stock No: 012601) and Ai14 (Gt(ROSA)26Sor$^{\text{tm14(CAG-tdTomato)Hze}}$)$^{+/+}$ (Jackson Laboratory - Stock No: 007914). This breeding scheme was used because the basal fluorescence of GFP in the LYVE1 EGFP-hCre mice is low[112]. No differences between the sexes were observed (data not shown), so males and females were pooled. Randomization was used for all animal grouping.

Histology

Mice were sacrificed via isoflurane overdose and perfused intracardially with heparinized-saline followed by 4% paraformaldehyde, unless otherwise noted. In some cases, the vasculature was labeled with perfusion of dye, FITC-albumin (Sigma Aldrich) or DiI (Life technologies) using the protocols described in[44,63], respectively. The heads were fixed in 4% paraformaldehyde for 24 hours, then decalcified for 48 hours in formic acid (4%) solution, and saturated in 30% sucrose for sectioning. Tissue sections of 100 micrometers thick were sectioned on a freezing microtome. Sections were then either stained for immunofluorescence or thionin-nissl. For immunofluorescence, primary antibodies (and their respective dilutions) used on tissue sections were as follows: OMP (WAKO, 1:500), NeuN (Millipore, 1:250), Aquaporin-1 (Santa Cruz, 1:250), Aquaporin-2 (Santa Cruz, 1:250), Aquaporin-3 (Santa Cruz, 1:250), Aquaporin-4 (Santa Cruz, 1:250), Aquaporin-5 (Santa Cruz, 1:250), Oligo1 (Santa Cruz, 1:250), CD164 (Santa Cruz, 1:250), MRC1 (Abcam, 1:500), and GFAP (Abcam, 1:500). The following secondary antibodies were purchased from Abcam and used at a 1:500 working dilution: Goat Anti-Rabbit IgG H&L (Alexa Fluor® 488), Donkey Anti-Goat IgG H&L (Alexa Fluor® 488), Goat Anti-Mouse IgG H&L (Alexa Fluor® 488), Donkey Anti-Rabbit IgG H&L (Alexa Fluor® 647), Donkey Anti-Goat IgG H&L (Alexa Fluor® 647), and Goat Anti-Mouse IgG H&L (Alexa Fluor® 647) preabsorbed. All staining was done in 24 well plates, with one section per well. Sections were first blocked in either 4% goat or donkey serum for one hour at room temperature, then incubated in a 4% serum/primary antibody solution overnight at 4°C. Sections were then incubated in a 4% serum/secondary antibody solution for one hour at room temperature. Sections were mounted on silane coated unifrost slides (Azer Scientific), then cover-slipped using fluoroshield mounting medium with DAPI (Abcam). Imaging was done on an Olympus Fluoview 1000 confocal, and images were processed in ImageJ (NIH). For thionin-nissl staining, sections were first mounted on silane-coated unifrost slides and allowed to dry overnight in a 37°C incubator. Slides were then immersed in 95% EtOH, 70% EtOH, 50% EtOH, distilled water, thionin-nissl staining solution, 50%, 70% EtOH, 95% EtOH, 100% EtOH, and xylene and coverslipped using Cytoseal (Thermofisher).

Cisterna magna (CM) injections

The animal was anesthetized with isoflurane in oxygen (5% induction, 2% maintainence). The dorsal surface of the head was elevated 8 mm above the back of the animal and the head was tilted downward at an angle of 10 degrees from horizontal. The base of the skull was exposed by an incision, and a fine glass-pipette (~20 micrometers in diameter for dye injections) or a 26G needle (for kaolin injections) was inserted into the cisterna magna using a stereotaxic instrument (Stoelting). Either 2.0µL of 2% Evans blue in aCSF (Tocris Bioscience) or 5.0µL of 10% solution of 3kDa-FITCDextran in aCSF was infused at a constant rate of 0.2 µL/min using a syringe pump (Harvard Apparatus), an infusion rate that does not raise ICP in mice[113]. After the injection, the animal was sacrificed via isoflurane overdose and perfused for histology. For kaolin injections, twenty microliters of 250 mg/mL kaolin (Sigma-Aldrich) in aCSF (Tocris Bioscience) was infused at a constant rate of 5.0 µL/min using a syringe pump (Harvard Apparatus). After the injection, the incision was sutured and the animal was monitored for 2 days until ICP measurements were made.

SeeDB clearing of the spinal column

A modified version of the SeeDB protocol[63,64] was used to clear the spinal column. The spinal columns were decalcified in formic acid (4%) solution for two days. Next, the spinal columns were saturated in a fructose and α-thioglycerol gradient: 20% - 8 hours, 40% - 12 hours, 60% - 24 hours, 80% - 24 hours, 100% - 48 hours, and SeeDB solution – 72 hours. Once cleared, the dorsal side of the spinal columns were imaged under a light microscope.

CT imaging of calcified tissue

Swiss Webster skulls were imaged with a GE v|tome|x L 300 high-resolution nano/microCT scanner and C57BL/6J skulls were imaged on an OMNI-X HD600 industrial microCT scanner (Varian Medical Systems). Scan settings were 100kV, 0.1mA (GE) or 160kV, 0.25 mA (Varian Medical Systems). Image stacks were processed and analyzed in Avizo 8. For each skull, a threshold that segmented the calcified and non-calcified tissue was chosen such that the zygotic maxillary suture, which is externally visible by eye, was clearly defined in the segmented image. To validate that the CT images accurately captured the fine details of the cribriform plate, in a subset of skulls the cranial vault was removed using a Dremel tool and the cribriform plate photographed on a Zeiss StereoDiscovery V8.

Intranasal administration of substances

After the mouse had been rendered unconscious by a brief exposure to isoflurane, 20μL of $ZnSO_4$ (10% in sterile H_2O) or vehicle control (sterile H_2O) was administered to the left nare with a blunt 32G needle. The animal was then inverted to allow for excess fluid to exit the nasal cavity. The animals were monitored and weighed daily after treatment. Approximately 4% of animals treated with $ZnSO_4$ died within 24 hours of administration.

Quantification of movement of Evans blue (EB) and olfactory bulb size

Images were obtained of the turbinates and olfactory bulb post-mortem in midline sagittally-sectioned $ZnSO_4$ and vehicle-treated mice using a Zeiss StereoDiscovery V8 with a 2000R scientific CCD camera (Retiga) utilizing μManager software[114]. We used the red channel, in which EB dye appears as a decrease in intensity, for all analyses. To measure the dye movement into the nasal epithelium, a rectangular ROI (5 mm rostral-caudal extent and 3 mm dorsal ventral) was placed with the caudal-dorsal corner located at the inflection point of the dorsal surface of the olfactory bulb. The center of mass, the location of maximal dye concentration (peak) along the rostral caudal axis, and the maximal dye value were quantified and plotted using Matlab. Using ImageJ, olfactory bulb ROIs were manually drawn around the outer edge of the olfactory bulb to quantify olfactory bulb size.

For quantifying dye movement along the spinal column, spinal columns were separated from the skull between the C2 and C3 vertebrae, cleared in SeeDB reagents, and photos of the dorsal side of the spinal columns were taken using a Zeiss StereoDiscovery V8 with a 2000R scientific CCD camera (Retiga) utilizing μManager software[114] (Fig. 9D top). Using ImageJ, the image was split into red, green, and blue channels, and only the red channel was used for analysis (Fig. 9D bottom). To compensate for the small bends present in the fixed spinal columns, for each spinal column, a line (yellow) was manually drawn along the midline, from the anterior to posterior end (Fig. 9D bottom). The dye intensity was measured along this line as a function of distance traveled down the spinal column (Fig. 9F).

Intracranial pressure (ICP) measurements

All surgical procedures were under isoflurane anesthesia (5% for induction and 2% for maintenance). A titanium head-bar was attached to the skull with cyanoacrylate glue and dental cement[115,116] and the skull was covered with a thin layer of cyanoacrylate glue. After two days of recovery, the animal was habituated to head fixation on a spherical treadmill for one day (for three 30-minute sessions). On the day of the ICP experiment (one day after the habituation), the mouse was anesthetized with isoflurane and a small craniotomy (~1 mm diameter) was made in the somatosensory cortex. A pressure measuring catheter (SPR-1000, Millar) was inserted into the cortex (-1.0 mm dorsal, -1 mm ventral from bregma), and a tight seal was made using Qwik-sil (World Precision Instruments). This surgical procedure took approximately 10 minutes. The animal was allowed to wake from anesthesia and to freely locomote on the spherical treadmill[75,117] for two hours, during which both intracranial pressure and locomotion were recorded simultaneously at 1 kHz (NI USB-6003). To minimize any residual effect of anesthesia on ICP[72], we only analyzed data collected more than 1 hour after the cessation of anesthesia.

Statistical analysis

Unless noted, all statistical analysis was performed using Matlab (R2015b, MathWorks, Natick, MA), with the Matlab function used (i.e. 'ttest2') is listed. All summary data were reported as the mean±standard deviation (SD). Normality (Anderson-Darling test, adtest) and of the samples were tested before statistical testing. When the data conform to the normality assumption, difference between treatments were compared using unpaired t-test (ttest2). If the condition of normality was not met, parametric tests (ttest2) were substituted with a non-parametric method (Mann-Whitney U test, ranksum). For comparing the effects of treatment and duration on CSF drainage, two-way ANOVA was used. For the wheel activity data, the K-S test was used. For the ICP data, a mixed model ANOVA test was used. A result was considered significant if $p \leq 0.05$ after correcting for multiple comparisons using the Bonferonni correction.

Acknowledgements: This work is supported by a Scholar Award from the McKnight Endowment Fund for Neuroscience, National Institutes of Health Grant R01NS078168, P01HD078233, and NSF grant CBET1705854 to P.J.D., and a Huck Graduate Enrichment Grant and F31NS105461 from the NIH to JNN. We thank B. Strowbridge for suggesting $ZnSO_4$, A. Shih and D. Hartman for assistance with SeeDB, J. Richtsmeier and members of the Drew lab for comments on the manuscript. All confocal imaging was done using the Penn State Microscopy and Cytometry Facility - University Park, PA.

Author Contributions: JNN designed research, performed experiments, and wrote the manuscript. DC and TMR performed CT imaging and analyzed data. QZ performed ICP experiments and analyzed data. AC performed histology experiments. PJD designed and supervised the research and wrote the manuscript.

Data Availability: The data that support the findings of this study are available from the corresponding author upon request.

Competing financial interests: The authors declare no competing financial interests.

References

1. Simon, M. J. & Iliff, J. J. Regulation of cerebrospinal fluid (CSF) flow in neurodegenerative, neurovascular and neuroinflammatory disease. *Biochim. Biophys. Acta - Mol. Basis Dis.* **1862,** 442–451 (2016).

2. Damkier, H. H., Brown, P. D. & Praetorius, J. Cerebrospinal fluid secretion by the choroid plexus. *Physiol. Rev.* **93,** 1847–92 (2013).

3. Iliff, J. J. *et al.* A Paravascular Pathway Facilitates CSF Flow Through the Brain Parenchyma and the Clearance of Interstitial Solutes, Including Amyloid . *Sci. Transl. Med.* **4,** 147ra111-147ra111 (2012).

4. Weed, L. H. The absorption of cerebrospinal fluid into the venous system. *Am. J. Anat.* **31,** 191–221 (1923).

5. McComb, J. G. Recent research into the nature of cerebrospinal fluid formation and absorption. *J. Neurosurg.* **59,** 369–383 (1983).

6. Zakharov, a. *et al.* Integrating the roles of extracranial lymphatics and intracranial veins in cerebrospinal fluid absorption in sheep. *Microvasc. Res.* **67,** 96–104 (2004).

7. Pollay, M. The function and structure of the cerebrospinal fluid outflow system. *Cerebrospinal Fluid Res.* **7,** 9 (2010).

8. May, C. *et al.* Cerebrospinal fluid production is reduced in healthy aging. *Neurology* **40,** 500–3 (1990).

9. de Leon, M. J. *et al.* CSF clearance in Alzheimer Disease measured with dynamic PET 2) Running title: Impaired CSF clearance in. *J. Nucl. Med.* **58,** 1471–1476 (2017).

10. Czosnyka M, Czosnyka Z, Momjian S, P. J. Cerebrospinal fluid dynamics. *Physiol Meas.* **25,** R51-76 (2004).

11. Albeck, M. J. *et al.* Age dependency of resistance to cerebrospinal fluid outflow. *J. Neurosurg.* **89,** 275–278 (1998).

12. König, K., Heissler, H. E., Zumkeller, M. & Rickels, E. Age-dependence of cerebrospinal parameters. *Acta Neurochir. Suppl.* 315–318 (2005). doi:10.1007/3-211-32318-X-65

13. Silverberg, G., Mayo, M., Saul, T., Fellmann, J. & McGuire, D. Elevated cerebrospinal fluid pressure in patients with Alzheimer's disease. *Cerebrospinal Fluid Res.* **3,** 7 (2006).

14. Kosteljanetz, M. Intracranial pressure: cerebrospinal fluid dynamics and pressure-volume relations. *Acta Neurol Scand Suppl* **111,** 1–23 (1987).

15. Marmarou, A., Shulman, K. & LaMorgese, J. Compartmental analysis of compliance and outflow resistance of the cerebrospinal fluid system. *J. Neurosurg.* **43,** 523–34 (1975).

16. Aspelund, A. *et al.* A dural lymphatic vascular system that drains brain interstitial fluid and macromolecules. **212,** 991–999 (2015).

17. Louveau, A. *et al.* Structural and functional features of central nervous system lymphatic vessels. *Nature* (2015). doi:10.1038/nature14432

18. Walter, B. A., Valera, V. A., Takahashi, S. & Ushiki, T. The olfactory route for cerebrospinal fluid drainage into the peripheral lymphatic system. *Neuropathol. Appl. Neurobiol.* **32,** 388–396 (2006).

19. Ma, Q. *et al.* Rapid lymphatic efflux limits cerebrospinal fluid flow to the brain. *Acta Neuropathol.* (2018). doi:10.1007/s00401-018-1916-x

20. Bradbury, M. W., Cserr, H. F. & Westrop, R. J. Drainage of cerebral interstitial fluid into deep cervical lymph of the rabbit. *Am. J. Physiol.* **240,** F329–F336 (1981).

21. Erlich, S. S., McComb, J. G., Hyman, S. & Weiss, M. H. Ultrastructural morphology of the olfactory pathway for cerebrospinal fluid drainage in the rabbit. *J. Neurosurg.* **64,** 466–473 (1986).

22. Yamada, S., DePasquale, M., Patlak, C. S. & Cserr, H. F. Albumin outflow into deep cervical lymph from different regions of rabbit brain. *Am. J. Physiol.* **261,** H1197–H1204 (1991).

23. Cserr, H. F. & Knopf, P. M. Cervical lymphatics, the blood-brain barrier and the immunoreactivity of the brain: a new view. *Immunol. Today* **13,** 507–512 (1992).

24. Weller, R. O., Kida, S. & Zhang, E. T. Pathways of fluid drainage from the brain--morphological aspects and immunological significance in rat and man. *Brain Pathol.* **2,** 277–284 (1992).

25. Kida, S., Pantazis, a & Weller, R. O. CSF drains directly from the subarachnoid space into nasal lymphatics in the rat. Anatomy, histology and immunological significance. *Neuropathol. Appl. Neurobiol.* **19,** 480–488 (1993).

26. Boulton, M. *et al.* Drainage of CSF through lymphatic pathways and arachnoid villi in sheep: measurement of 125I-albumin clearance. *Neuropathol. Appl. Neurobiol.* **22,** 325–333 (1996).

27. Johnston, M., Zakharov, A., Papaiconomou, C., Salmasi, G. & Armstrong, D. Evidence of connections between cerebrospinal fluid and nasal lymphatic vessels in humans, non-human primates and other mammalian species. *Cerebrospinal Fluid Res.* **1,** 2 (2004).

28. Bradbury, B. Y. M. W. B. & Cole, D. F. The Role of the Lymphatic System in Drainage of Cerebrospinal Fluid and Aqueous Humour. *J Physiol* **299,** 353–365 (1980).

29. Szentistvanyi, I. & Patlak, C. Drainage of interstitial fluid from different regions of rat brain. *Am. J. Physiol.* **246,** F835-844 (1984).

30. Sykova, E. & Nicholson, C. Diffusion in Brain Extracellular Space. *Physiol. Rev.* **88,** 1277–1340 (2008).

31. Mollanji, R., Bozanovic-Sosic, R., Zakharov, A., Makarian, L. & Johnston, M. G. Blocking cerebrospinal fluid absorption through the cribriform plate increases resting intracranial pressure. *Am. J. Physiol. Regul. Integr. Comp. Physiol.* **282,** R1593-9 (2002).

32. Silver, I., Kim, C., Mollanji, R. & Johnston, M. Cerebrospinal fluid outflow resistance in sheep: Impact of blocking cerebrospinal fluid transport through the cribriform plate. *Neuropathol. Appl. Neurobiol.* **28,** 67–74 (2002).

33. Ethell, D. W. Disruption of cerebrospinal fluid flow through the olfactory system may contribute to Alzheimer's disease pathogenesis. *J. Alzheimer's Dis.* **41,** 1021–1030 (2014).

34. Gaurav S. Ajmani, Helen H. Suh, and J. M. P. Effects of Ambient Air Pollution Exposure on Olfaction: A Review. *Environ. Health Perspect.* **124,** 1683–1693 (2016).

35. Kalmey, J. K., Thewissen, J. G. M. & Dluzen, D. E. Age-related size reduction of foramina in the cribriform plate. *Anat. Rec.* **251,** 326–329 (1998).

36. Pihlstrom, H., Fortelius, M., Hemila, S., Forsman, R. & Reuter, T. Scaling of mammalian ethmoid bones can predict olfactory organ size and performance. *Proc. R. Soc. B Biol. Sci.* **272,** 957–962 (2005).

37. Bhatnagar, K. P. & Kallen, F. C. Cribriform plate of ethmoid, olfactory bulb and olfactory acuity in forty species of bats. *J. Morphol.* (1974). doi:10.1002/jmor.1051420104

38. Bird, D. J., Amirkhanian, A., Pang, B. & Van Valkenburgh, B. Quantifying the Cribriform Plate: Influences of Allometry, Function, and Phylogeny in Carnivora. *Anat. Rec.* **297,** 2080–2092 (2014).

39. Bird, D. J. *et al.* Olfaction written in bone: cribriform plate size parallels olfactory receptor gene repertoires in Mammalia. *Proc. R. Soc. B Biol. Sci.* **285,** 20180100 (2018).

40. Al Kawas, S., Amizuka, N., Bergeron, J. J. M. & Warshawsky, H. Immunolocalization of the cation-independent mannose 6-phosphate receptor and cathepsin B in the enamel organ and alveolar bone of the rat incisor. *Calcif. Tissue Int.* **59,** 192–199 (1996).

41. Naruse, I. & Ueta, E. Hydrocephalus manifestation in the genetic polydactyly/ arhinencephaly mouse (Pdn/Pdn). *Congenit. Anom. (Kyoto).* **42,** 27–31 (2002).

42. Buiakova, O. I. *et al.* Olfactory marker protein (OMP) gene deletion causes altered physiological activity of olfactory sensory neurons. *Proc. Natl. Acad. Sci. U. S. A.* **93,** 9858–9863 (1996).

43. Ekberg, J. A. K. *et al.* OMP-ZsGreen fluorescent protein transgenic mice for visualisation of olfactory sensory neurons in vivo and in vitro. *J. Neurosci. Methods* **196,** 88–98 (2011).

44. Tsai, P. S. *et al.* Correlations of neuronal and microvascular densities in murine cortex revealed by direct counting and colocalization of nuclei and vessels. *J. Neurosci.* **29,** 14553–14570 (2009).

45. Yiwen Li1, Ying Song2, Lian Zhao2, Gabriel Gaidosh1, Alan M Laties2, and R. W. Direct labeling and visualization of blood vessels with lipophilic carbocyanine dye DiI. **4,** 1703–1708 (2008).

46. Knudsen, F. W., Andersen, M. & Krag, C. The arterial supply of the clavicle. *Surg. Radiol. Anat.* **11,** 211–214 (1989).

47. Yang, Y. X., Lu, Q. K., Liao, J. C. & Dang, R. S. Morphological characteristics of the anterior ethmoidal artery in ethmoid roof and endoscopic localization. *Skull Base* **19,** 311–317 (2009).

48. Souza, S. A., Souza, M. M. A. de, Gregório, L. C. & Ajzen, S. Anterior ethmoidal artery evaluation on coronal CT scans. *Braz. J. Otorhinolaryngol.* **75,** 101–106 (2009).

49. Takata, K., Matsuzaki, T. & Tajika, Y. Aquaporins: Water channel proteins of the cell membrane. *Prog. Histochem. Cytochem.* **39,** 1–83 (2004).

50. Verkman, A. S., Tradtrantip, L., Smith, A. J. & Yao, X. Aquaporin Water Channels and Hydrocephalus. *Pediatr. Neurosurg.* (2016). doi:10.1159/000452168

51. Sakai, H. *et al.* Distribution of aquaporin genes and selection of individual reference genes for quantitative real-time RT-PCR analysis in multiple tissues of the mouse. *Can J Physiol Pharmacol.* **92,** 789–796 (2014).

52. Procino, G. *et al.* AQP5 is expressed in type-B intercalated cells in the collecting duct system of the rat, mouse and human kidney. *Cell. Physiol. Biochem.* **28,** 683–692 (2011).

53. Shields, S. D., Moore, K. D., Phelps, P. E. & Basbaum, A. I. Olfactory ensheathing glia express aquaporin 1. *J. Comp. Neurol.* **518,** 4329–4341 (2010).

54. Ablimit A, Matsuzaki T, Tajika Y, Aoki T, Hagiwara H, T. K. Immunolocalization of water channel aquaporins in the nasal olfactory mucosa. *Arch Histol Cytol.* **69,** 1–12 (2006).

55. Nielsen, S. *et al.* Specialized membrane domains for water transport in glial cells: high-resolution

immunogold cytochemistry of aquaporin-4 in rat brain. *J. Neurosci.* **17,** 171–180 (1997).

56. Smith, A. J., Yao, X., Dix, J. A., Jin, B. J. & Verkman, A. S. Test of the 'glymphatic' hypothesis demonstrates diffusive and aquaporin-4-independent solute transport in rodent brain parenchyma. *Elife* **6,** 1–16 (2017).

57. Wulf, E., Deboben, a, Bautz, F. a, Faulstich, H. & Wieland, T. Fluorescent phallotoxin, a tool for the visualization of cellular actin. *Proc. Natl. Acad. Sci. U. S. A.* **76,** 4498–4502 (1979).

58. Wang, Y. *et al.* In vivo albumin labeling and lymphatic imaging. *Proc. Natl. Acad. Sci. U. S. A.* **112,** 208–213 (2014).

59. Maloveska, M. *et al.* Dynamics of Evans blue clearance from cerebrospinal fluid into meningeal lymphatic vessels and deep cervical lymph nodes. *Neurol. Res.* **6412,** 1–9 (2018).

60. Harrell, M. I., Iritani, B. M. & Ruddell, A. Lymph node mapping in the mouse. *J. Immunol. Methods* **332,** 170–174 (2008).

61. Leinenga, G., Langton, C., Nisbet, R. & Götz, J. Ultrasound treatment of neurological diseases — current and emerging applications. *Nat. Rev. Neurol.* **12,** 161–174 (2016).

62. Redzic, Z. B., Preston, J. E., Duncan, J. A., Chodobski, A. & Szmydynger-Chodobska, J. The Choroid Plexus - Cerebrospinal Fluid System: From Development to Aging. *Curr. Top. Dev. Biol.* **71,** 1–52 (2005).

63. Ke, M.-T., Fujimoto, S. & Imai, T. technical reports SeeDB : a simple and morphology-preserving optical clearing agent for neuronal circuit reconstruction. *Nat. Publ. Gr.* **16,** 1154–1161 (2013).

64. Hartmann, D. a. *et al.* Pericyte structure and distribution in the cerebral cortex revealed by high-resolution imaging of transgenic mice. *Neurophotonics* **2,** 041402 (2015).

65. Cserr, H. F., Harling-Berg, C. J. & Knopf, P. M. Drainage of brain extracellular fluid into blood and deep cervical lymph and its immunological significance. *Brain Pathol.* **2,** 269–276 (1992).

66. Michelle Pizzo , Daniel J Wolak , Niyanta N Kumar , Eric Brunette , Christina L Brunnquell , Melanie-Jane Hannocks , N Joan Abbott , M Elizabeth Meyerand , Lydia Sorokin , Danica B Stanimirovic, R. T. Intrathecal antibody distribution in the rat brain: surface diffusion, perivascular transport, and osmotic enhancement of delivery. *J. Physiol.* **596,** 445–475 (2018).

67. Hubbs, A. F. *et al.* Respiratory and olfactory cytotoxicity of inhaled 2,3-pentanedione in sprague-dawley rats. *Am. J. Pathol.* **181,** 829–844 (2012).

68. Burd, G. D. Morphological Study of the Effects of Intranasal Zinc Sulfate Irrigation on the Mouse Olfactory Epithelium and Olfactory Bulb. *Microsc. Res. Tech.* **24,** 195–213 (1993).

69. McBride, K., Slotnick, B. & Margolis, F. L. Does intranasal application of zinc sulfate produce anosmia in the mouse? An olfactometric and anatomical study. *Chem. Senses* **28,** 659–670 (2003).

70. Stewart WB, Greer CA, T. M. The effect of intranasal zinc sulfate treatment on odor-mediated behavior and on odor-induced metabolic activity in the olfactory bulbs of neonatal rats. *Brain Res.* **284,** 247–59 (1983).

71. Jones, H. C. Cerebrospinal fluid pressure and resistance to absorption during development in normal and hydrocephalic mutant mice. *Exp. Neurol.* **90,** 162–172 (1985).

72. Gao, Y.-R. & Drew, P. J. Effects of Voluntary Locomotion and Calcitonin Gene-Related Peptide on the Dynamics of Single Dural Vessels in Awake Mice. *J. Neurosci.* **36,** 2503–2516 (2016).

73. Gao, Y. R. *et al.* Time to wake up: Studying neurovascular coupling and brain-wide circuit function in the un-anesthetized animal. *Neuroimage* **153,** 382–398 (2017).

74. Gao, Y. R. & Drew, P. J. Determination of vessel cross-sectional area by thresholding in Radon space. *J. Cereb. Blood Flow Metab.* **34,** 1180–1187 (2014).

75. Huo, B.-X. B.-X., Smith, J. B. & Drew, P. J. Neurovascular coupling and decoupling in the cortex during voluntary locomotion. *J. Neurosci.* **34,** 10975–81 (2014).

76. Dickinson, M. E. *et al.* High-throughput discovery of novel developmental phenotypes. *Nature* **537,** 508–514 (2016).

77. Bloch, O., Auguste, K. I., Manley, G. T. & Verkman, a S. Accelerated progression of kaolin-induced hydrocephalus in aquaporin-4-deficient mice. *J. Cereb. Blood Flow Metab.* **26,** 1527–37 (2006).

78. Shirey, M. J. *et al.* Brief anesthesia, but not voluntary locomotion, significantly alters cortical temperature. *J. Neurophysiol.* **114,** 309–322 (2015).

79. Nagelhus, E. a & Ottersen, O. P. Physiological roles of aquaporin-4 in brain. *Physiol. Rev.* **93,** 1543–62 (2013).

80. Lindvall, M., Edvinsson, L. & Owman, C. Sympathetic nervous control of cerebrospinal fluid production from the choroid plexus. *Science* **201,** 176–178 (1978).

81. Edvinsson, L. & Lindvall, M. Autonomic vascular innervation and vasomotor reactivity in the choroid plexus. *Exp. Neurol.* **62,** 394–404 (1978).

82. Edvinsson, L. Neuropeptide Y and the cerebral circulation. *NPY Fam. Pept. Neurobiol. Cardiovasc. Metab. Disord. from Genes to Ther.* 105–112 (2006).

83. Umans, B. D. & Liberles, S. D. Neural Sensing of Organ Volume. *Trends Neurosci.* **41,** 911–924 (2018).

84. Sarah-Jane Guild, Utkarsh Saxena, Fiona McBryde, S. C. M. and R. R. INTRACRANIAL PRESSURE INFLUENCES THE LEVEL OF SYMPATHETIC TONE. *Am. J. Physiol. Integr. Comp. Physiol.* 1–10 (2018). doi:10.1152/ajpregu.00183.2018

85. Jalalvand, E. *et al.* Cerebrospinal fluid-contacting neurons sense pH changes and motion in the hypothalamus. *J. Neurosci.* 3359–17 (2018). doi:10.1523/JNEUROSCI.3359-17.2018

86. Hoff, J. T. & Reis, D. J. Localization of Regions Mediating the Cushing Response in CNS of Cat. *Arch. Neurol.* **23,** 228–240 (1970).

87. Doba, N. & Reis, D. J. Localization within the lower brainstem of a receptive area mediating the pressor response to increased intracranial pressure (the Cushing response). *Brain Res.* **47,** 487–491 (1972).

88. M. W. B. BRADBURY* AND R. J. WESTROP. Factors Influencing Exit of Substances From Cerebrospinal Fluid into Deep Cervical Lymph of the Rabbit. 519–534 (1983).

89. Koh, L. *et al.* Development of cerebrospinal fluid absorption sites in the pig and rat: connections between the subarachnoid space and lymphatic vessels in the olfactory turbinates. *Anat. Embryol. (Berl).* **211,** 335–344 (2006).

90. Nagra, G., Koh, L., Zakharov, A., Armstrong, D. & Johnston, M. Quantification of cerebrospinal fluid transport across the cribriform plate into lymphatics in rats. *Am. J. Physiol. Regul. Integr. Comp. Physiol.* **291,** R1383–R1389 (2006).

91. Ma, Q., Ineichen, B. V., Detmar, M. & Proulx, S. T. Outflow of cerebrospinal fluid is predominantly

through lymphatic vessels and is reduced in aged mice. *Nat. Commun.* **8,** (2017).

92. CSERR, H. F. & PATLAK, C. S. in *Handbook of Experimental Pharmacology* **103,** 245–258 (1992).

93. Papaiconomou, C., Bozanovic-Sosic, R., Zakharov, a & Johnston, M. Does neonatal cerebrospinal fluid absorption occur via arachnoid projections or extracranial lymphatics? *Am. J. Physiol. Regul. Integr. Comp. Physiol.* **283,** R869–R876 (2002).

94. Johnston, M., Zakharov, A., Koh, L. & Armstrong, D. Subarachnoid injection of Microfil reveals connections between cerebrospinal fluid and nasal lymphatics in the non-human primate. *Neuropathol. Appl. Neurobiol.* **31,** 632–640 (2005).

95. Doty, R. L. & Kamath, V. The influences of age on olfaction: A review. *Front. Psychol.* **5,** 1–20 (2014).

96. Murphy, C. *et al.* Prevalence of olfactory impairment in older adults. *JAMA* **288,** 2307–2312 (2002).

97. Talamo, B. R. Pathological changes in olfactory neurons in patients with Alzheimer's disease. (1989).

98. Talamo, B. R. *et al.* Pathologic changes in olfactory neurons in Alzheimer's disease. *Ann.N.Y.Acad.Sci.* **640,** 1–7 (1991).

99. Kovács, T. Mechanisms of olfactory dysfunction in aging and neurodegenerative disorders. *Ageing Res. Rev.* **3,** 215–232 (2004).

100. Roberts, R. O. *et al.* Association Between Olfactory Dysfunction and Amnestic Mild Cognitive Impairment and Alzheimer Disease Dementia. *JAMA Neurol.* **55905,** 1 (2015).

101. Zou, Y. & Lu, Da, Liu LP, Zhang HH, Z. Y. Olfactory dysfunction in Alzheimer's disease. *Neuropsychiatr Dis Treat.* **12,** 869–875 (2016).

102. Doty, R. L. & Hastings, L. Neurotoxic Exposure and Olfactory Impairment. *Clin. Occup. Environ. Med.* **1,** 547–575 (2001).

103. Adams, D. R. *et al.* Nitrogen dioxide pollution exposure is associated with olfactory dysfunction in older U.S. adults. *Int. Forum Allergy Rhinol.* 1–8 (2016). doi:10.1002/alr.21829

104. Imamura, F. & Hasegawa-Ishii, S. Environmental Toxicants-Induced Immune Responses in the Olfactory Mucosa. *Front. Immunol.* **7,** 1–7 (2016).

105. Cheng, H. *et al.* Nanoscale particulate matter from urban traffic rapidly induces oxidative stress and inflammation in olfactory epithelium with concomitant effects on brain. *Environ. Health Perspect.* **124,** 1537–1546 (2016).

106. Calderón-Garcidueñas, L. *et al.* Brain inflammation and Alzheimer's-like pathology in individuals exposed to severe air pollution. *Toxicol. Pathol.* **32,** 650–658 (2004).

107. Calderón-Garcidueas, L. *et al.* Neuroinflammation, hyperphosphorylated tau, diffuse amyloid plaques, and down-regulation of the cellular prion protein in air pollution exposed children and young adults. *J. Alzheimer's Dis.* **28,** 93–107 (2012).

108. Calderón-Garcidueñas, L. *et al.* Interactive and additive influences of Gender, BMI and Apolipoprotein 4 on cognition in children chronically exposed to high concentrations of PM2.5and ozone. APOE 4 females are at highest risk in Mexico City. *Environ. Res.* **150,** 411–422 (2016).

109. Calderón-Garcidueñas, L. *et al.* Prefrontal white matter pathology in air pollution exposed Mexico City young urbanites and their potential impact on neurovascular unit dysfunction and the development of Alzheimer's disease. *Environ. Res.* **146,** 404–417 (2016).

110. Chen, H. *et al.* Living near major roads and the incidence of dementia, Parkinson's disease, and multiple sclerosis: a population-based cohort study. *Lancet* **389,** 718–726 (2017).

111. Chen, H. *et al.* Exposure to ambient air pollution and the incidence of dementia: A population-based cohort study. *Environ. Int.* **108,** 271–277 (2017).

112. Pham, T. H. M. *et al.* Lymphatic endothelial cell sphingosine kinase activity is required for lymphocyte egress and lymphatic patterning. *J. Exp. Med.* **207,** 17–27 (2010).

113. Yang, L. *et al.* Evaluating glymphatic pathway function utilizing clinically relevant intrathecal infusion of CSF tracer. *J. Transl. Med.* **11,** 107 (2013).

114. Edelstein, A. D. *et al.* Advanced methods of microscope control using μManager software. *J. Biol. Methods* **1,** 10 (2014).

115. Drew, P. J. *et al.* Chronic optical access through a polished and reinforced thinned skull. *Nat. Methods* **7,** 981–4 (2010).

116. Shih, A. Y., Mateo, C., Drew, P. J., Tsai, P. S. & Kleinfeld, D. A Polished and Reinforced Thinned-skull Window for Long-term Imaging of the Mouse Brain. *J. Vis. Exp.* 4–9 (2012). doi:10.3791/3742

117. Huo, B. X., Gao, Y. R. & Drew, P. J. Quantitative separation of arterial and venous cerebral blood volume increases during voluntary locomotion. *Neuroimage* **105,** 369–379 (2015).

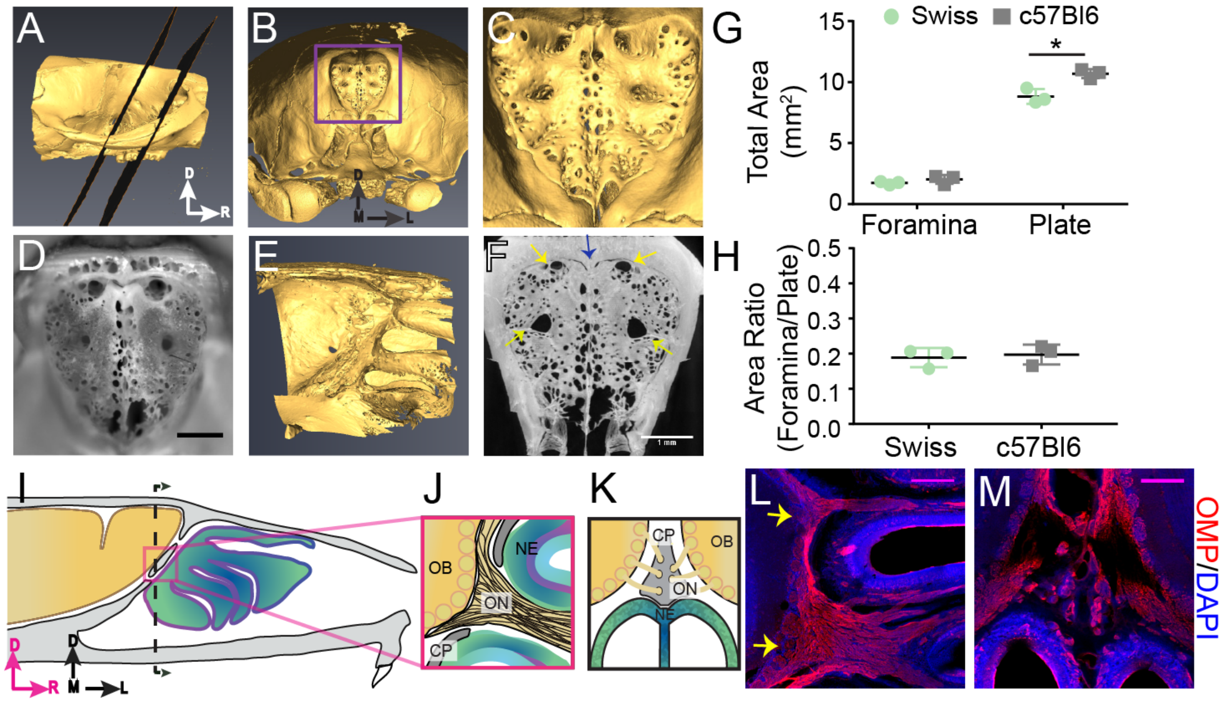

Figure 1: Structure of the calcified tissue of the cribriform plate and its relationship to olfactory sensory neuron axons. For schematics: olfactory nerve (ON), neuroepithelium (NE), cribriform plate (CP), olfactory bulb (OB) and glomeruli (yellow circles). D=dorsal, R=rostral, M=medial, and L=lateral. **A)** Sagittal view of a microCT scan of a mouse skull. Black planes bracket the area of the CP. **B)** Anterior-looking view of the CP from microCT image. **C)** Area indicated by purple box in **(B). D)** Photograph of the CP from the same point of view as the CT reconstruction in **(C)**. Scale bar 1 mm. **E)** Sagittal view of the OB and CP junction illustrating the curved structure of the CP. **F)** Max intensity projection of a 1.67 mm thick section of the CP depicting the major foramina (yellow arrows) and crista galli (blue arrow). Scale bar 1 mm. **G-H)** Mean ± standard deviation plotted. Circles and squares represent means of individual animals. **G)** Left: Comparison of total foramina area between Swiss Webster and C57BL/6J mice: (t(4) = 1.32, p = 0.256, n=3 for each group, ttest2). Comparison of the total area of the CP between Swiss Webster and C57BL/6J mice: (t(4) = 4.55, p = 0.021, n = 3 for each group, ttest2). (*p≤0.05). **H)** Comparison of the ratio of the foramina area and CP area between Swiss Webster and C57BL/6J mice: (t(4) = 0.3891, p = 0.7170, n=3 for each group, ttest2). **I)** Schematic of the sagittal plane of the mouse skull and brain showing the relationship of the OB and nerve junction to the CP. **J)** Sagittal view of the area within the pink box in **(I)**, depicting OSNs crossing the CP and terminating in the OB and glomeruli. **K)** Coronal view of the black dashed line in **(I)** illustrating the location of the CP relative to the OBs and NE. **L-M)** Immunofluorescent staining, OMP (red) and DAPI (blue). Scale bars 250 µm. **L)** Sagittal plane, area depicted in **(J),** showing the two main OSN axon bundles (yellow arrows) that pass through the major foramina of the CP. **M)** Coronal plane, area indicated in **(K),** showing OSN axon bundles that traverse the minor foramina of the CP along the crista galli.

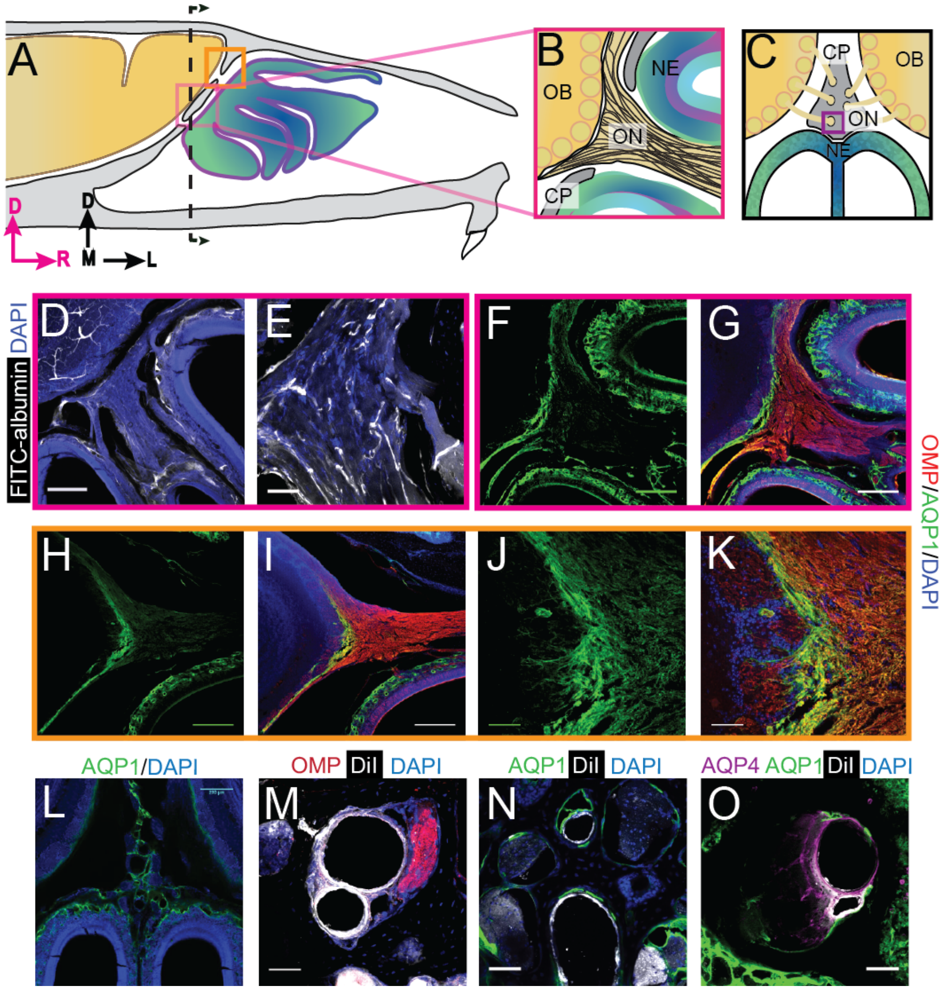

Figure 2: Aquaporin 1 and blood vessels are present in the cribriform plate and olfactory nerve junction. For schematics: olfactory nerve (ON), neuroepithelium (NE), cribriform plate (CP), olfactory bulb (OB) and glomeruli (yellow circles). D=dorsal, R=rostral, M=medial, and L=lateral). **A)** Schematic of the sagittal plane of the mouse skull and brain showing the relationship of the OB and nerve junction to the CP. **B)** Sagittal view of the area within the pink box in **(A)**, depicting OSNs crossing the CP and terminating in the OB and glomeruli. **C)** Coronal view of the black dashed line in **(A)** illustrating the location of the CP relative to the OBs and NE. **D)** Area depicted by the pink box in **(A)**, showing the presence of FITC-albumin (white) filled blood vessels along the medial ON. **E)** Magnified area of **(D)**. **F-O)** Immunofluorescent staining, OMP (red), AQP1 (green), AQP4 (purple), DiI (white), and DAPI (blue). **F-G)** Area depicted by the pink box in **(A),** showing the expression of AQP1 **(F)** at the junction of the OB and medial ON and in the lamina propria of the NE. **H-I)** Area depicted by the orange box in **(A),** showing the expression of AQP1 at the junction of the OB and lateral ON and in the lamina propria of the NE. **J-K)** Magnified area of **(H-I)**. **L)** AQP1 expression, in the area indicated in **(C)**, is present in the lining of the smaller foramina along the midline of the crista galli, on the olfactory nerve layer of the OB, and in the lamina propria of the NE**. M-O)** DiI labeled endothelial cells of blood vessels traversing the smaller foramina of the CP alongside ONs **(M)** and lined with AQP-1 **(N-O)** or AQP-4 **(O)**, area indicated by purple box in **(C). D, F-I, L)** Scale bars 250 μm. **E, J-K, M-O)** Scale bars 50 μm.

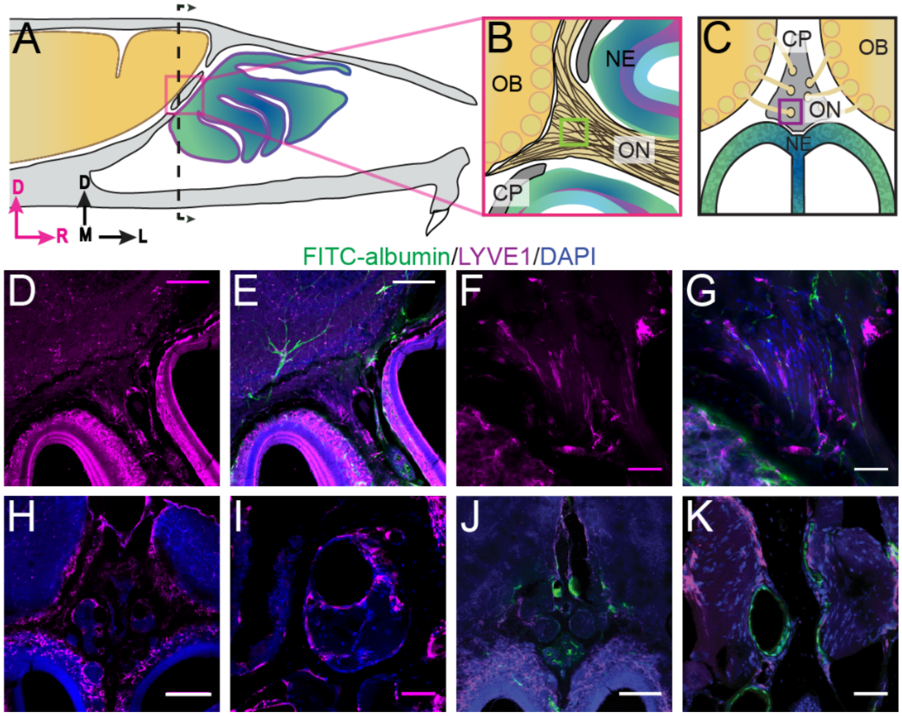

Figure 3: Localization of lymphatic vessels at the cribriform plate and olfactory bulb junction. For schematics: olfactory nerve (ON), neuroepithelium (NE), cribriform plate (CP), olfactory bulb (OB) and glomeruli (yellow circles). D=dorsal, R=rostral, M=medial, and L=lateral. **A)** Schematic of the sagittal plane of the mouse skull and brain showing the relationship of the OB and nerve junction to the CP. **B)** Sagittal view of the area within the pink box in **(A)**, depicting OSNs crossing the CP and terminating in the OB and glomeruli. **C)** Coronal view of the black dashed line in **(A)** illustrating the location of the CP relative to the OBs and NE. **D-K)** Immunofluorescent staining: LYVE1 (magenta), FITC-albumin (green), and DAPI (blue) in LYVE1-tdtomato mice. **D-E)** Localization of LYVE1^{+} vessels along the medial olfactory nerve, sagittal area indicated in **(B),** depicting LYVE1^{+}/FITC-albumin negative vessels (putative lymphatic vessels) running parallel to the olfactory nerve. **F-G)** Area indicated by green box in **(B)**, magnified area of **(D-E)**. **H)** Localization of LYVE1^{+} vessels in the nasal epithelium and traversing the CP, coronal area indicated in **(C)**. **I)** Area indicated by purple box in **(C)**, magnified area of **(H),** depicting LYVE1^{+} vessels traversing foramina of the CP. **J)** Localization of LYVE1^{+} vessels and blood vessels (FITC-albumin) in the nasal epithelium and traversing the CP, coronal area indicated in **(C). K)** Area indicated by purple box in **(C)**, magnified area of **(H),** depicting only blood vessels (labeled with FITC-albumin) traversing foramina of the CP. **D-E, H, J)** Scale bars 250 µm. **F-G, I, K)** Scale bars 50 µm.

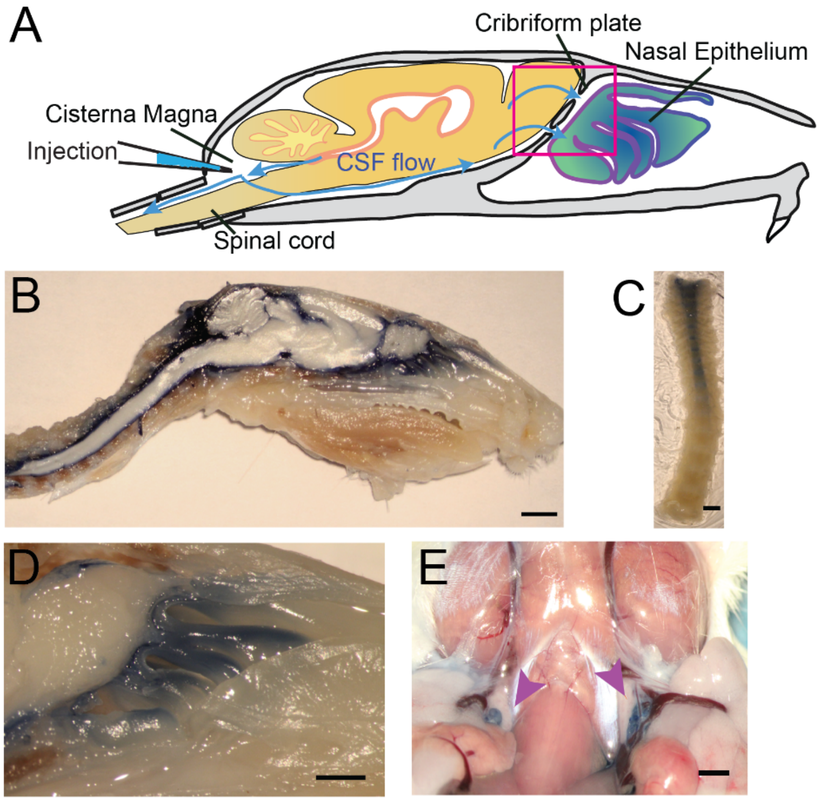

Figure 4: Visualization of CSF flow into the nasal cavity and spinal column by injection of Evans blue dye into the cisterna magna. A) Schematic of the sagittal plane of the mouse skull and brain depicting the flow of CSF (blue arrows) and location of EB injection into the cisterna magna. **B)** Sagittal, midline cut of a decalcified skull and spinal column after a cisterna magna EB injection. Scale bar 3mm. **C)** A decalcified and SeeDB-cleared spinal column (cut between C2 and C3, with C3 at the top of the picture) after a cisterna magna EB injection. Scale bar 2 mm. **D)** Area depicted by pink box in **(A)**, showing drainage of EB dye across the CP into the nasal cavity. Scale bar 1 mm. **E)** Localization of EB dye in the deep cervical lymph nodes (purple arrows) after a cisterna magna EB injection. Scale bar 1 mm.

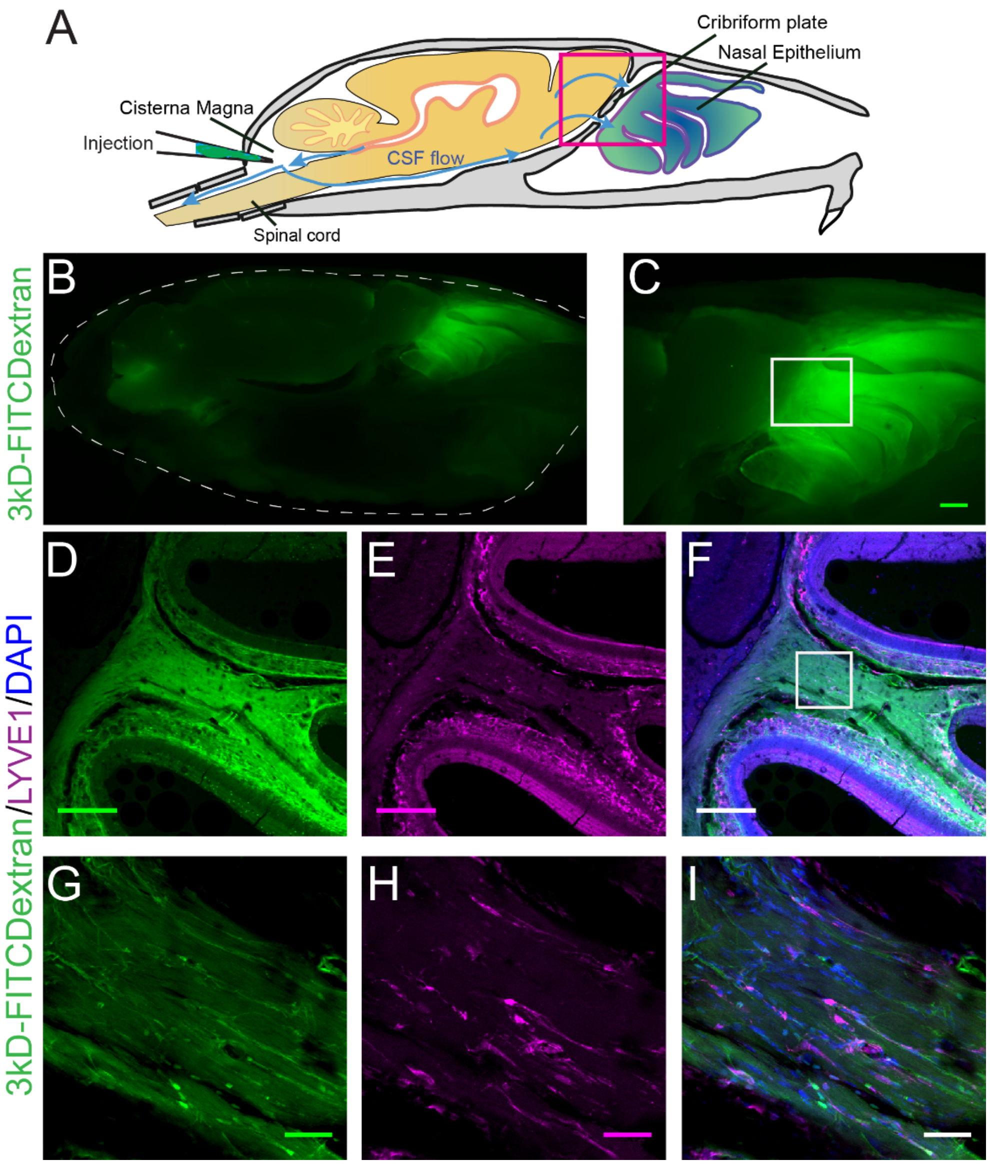

Figure 5: Visualization of CSF flow into the nasal cavity by injection of 3kDa-FITCDextran into the cisterna magna. A) Schematic of the sagittal plane of the mouse skull and brain depicting the flow of CSF (blue arrows) and location of 3kDa-FITCDextran injection into the cisterna magna. **B-I)** Fluorescent images of a mouse skull and brain 35 minutes after a 3kDa-FITCDextran (green) cisterna magna injection. **B)** Skull outlined by white dashed lines. 3kDa-FITCDextran is observed in the cisterna magna and the nasal cavity. **C)** Area indicated by pink box in **(A)**. FITC 3kD-Dextran is observed in the nasal cavity. Scale bar 500 µm. **D-I)** Fluorescent images of a mouse skull and brain 35 minutes after a 3kDa-FITCDextran (green) cisterna magna injection into a LYVE1-tdTomato (Ai14) mouse. LYVE1 (magenta) and DAPI (blue). **D-F)** Area indicated by white box in **(C)**. 3kDa-FITCDextran is observed draining into the nasal cavity along the olfactory nerve. LYVE1+ vessels are observed running parallel to the olfactory nerve. Scale bar 250 µm **G-I)** Area indicated by white box in (F). FITC 3kD-Dextran is observed moving along and through LYVE1+ vessels. Scale bar 50 µm.

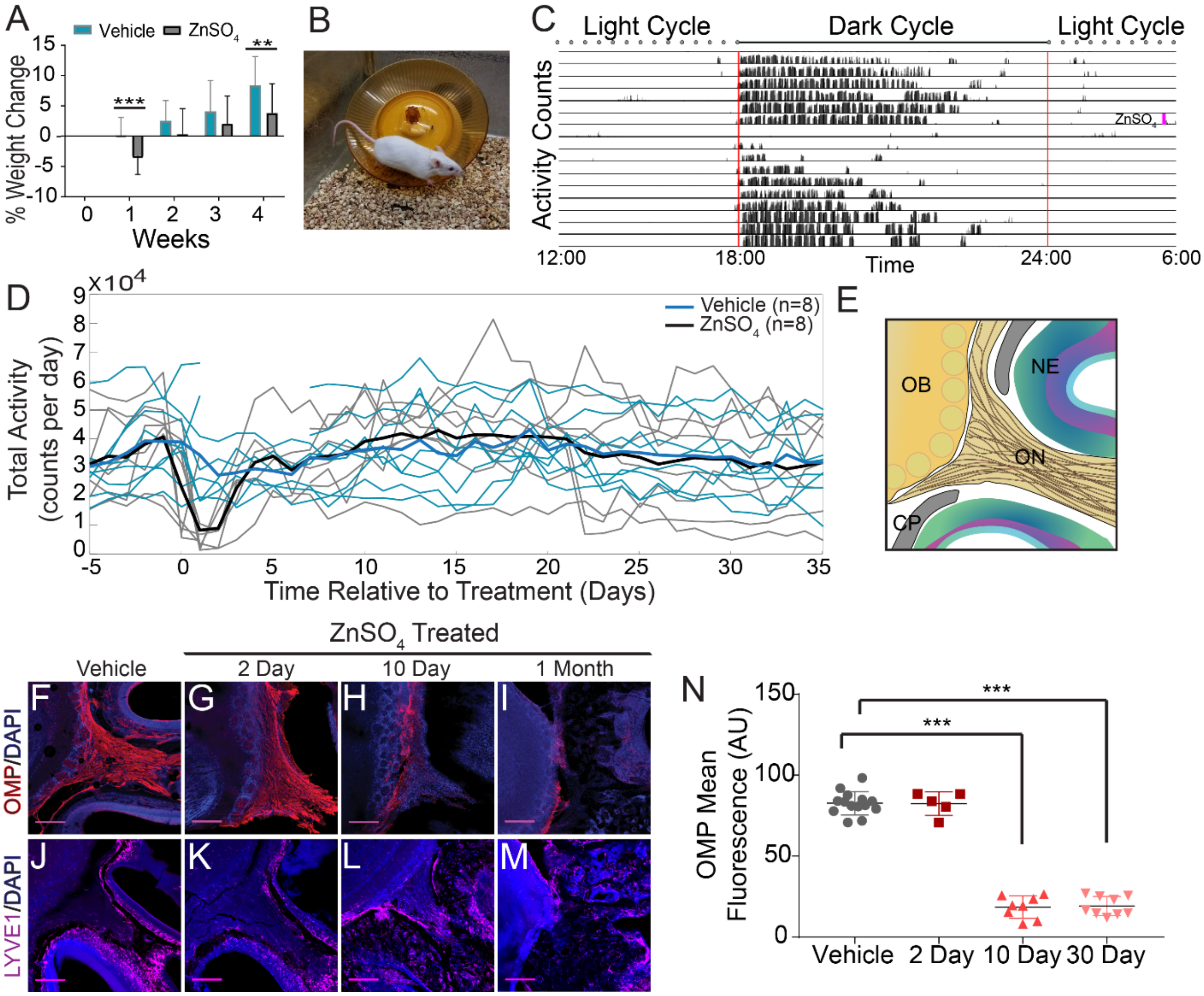

Figure 6: Effects of $ZnSO_4$ treatment on behavior and OSNs. A) Percent weight loss of vehicle (blue) and $ZnSO_4$ treated (black) mice after treatment. There was a significant difference in weight of $ZnSO_4$ treated mice compared to control mice 1 week ($p = 0.001$, $n = 17$ for vehicle and $n = 25$ for treated, ttest2) and 4 weeks ($p = 0.004$, $n = 17$ for vehicle and $n = 25$ for treated, ttest2) after treatment. Mean ± standard deviation plotted. $^{**}p \leq 0.01$ $^{***}p \leq 0.001$ **B)** Photo of a Swiss Webster mouse on the running wheel. **C)** Actogram of the activity of a single mouse before and after $ZnSO_4$ treatment. Treatment time indicated by pink line. **D)** Individual counts of total wheel activity per day (vehicle = blue, $ZnSO_4$ treated = gray), bold line is the mean of each group. No significant difference observed between groups ($p = 0.5189$, KSTAT = 0.3750, $n = 8$ for each group, K-S test). **E)** Schematic: sagittal plane depicting OSNs crossing the CP and synapsing onto the OB and glomeruli (yellow circles). **F-M)** Immunofluorescent staining of area depicted in **(E),** OMP (red), LYVE1 (magenta) and DAPI (blue). Scale bar 250 µm. **F, J)** Vehicle Control. **G, K)** Two days after $ZnSO_4$ treatment. **H, L)** Ten days after $ZnSO_4$ treatment. **I, M)** Thirty days after $ZnSO_4$ treatment. Swiss Webster mice were used for **(F-I)** and LYVE1-GFP (Ai6) mice were used for **(J–M)**. **N)** Quantification of OMP signal fluorescence for vehicle ($n = 14$) mice compared to 2 ($t(8) = 0.1429$, $p = 0.8898$, $n = 5$, post-hoc ttest2), 10 ($t(13) = 15.71$, $p \leq 0.001$, $n = 8$, post-hoc ttest2) and 30 ($t(13) = 25.39$, $p \leq 0.001$, $n = 9$, post-hoc ttest2) day $ZnSO_4$ treated mice. Mean ± standard deviation plotted. Circles, triangles, and squares represent means of individual animals. $^{***}p \leq 0.001$

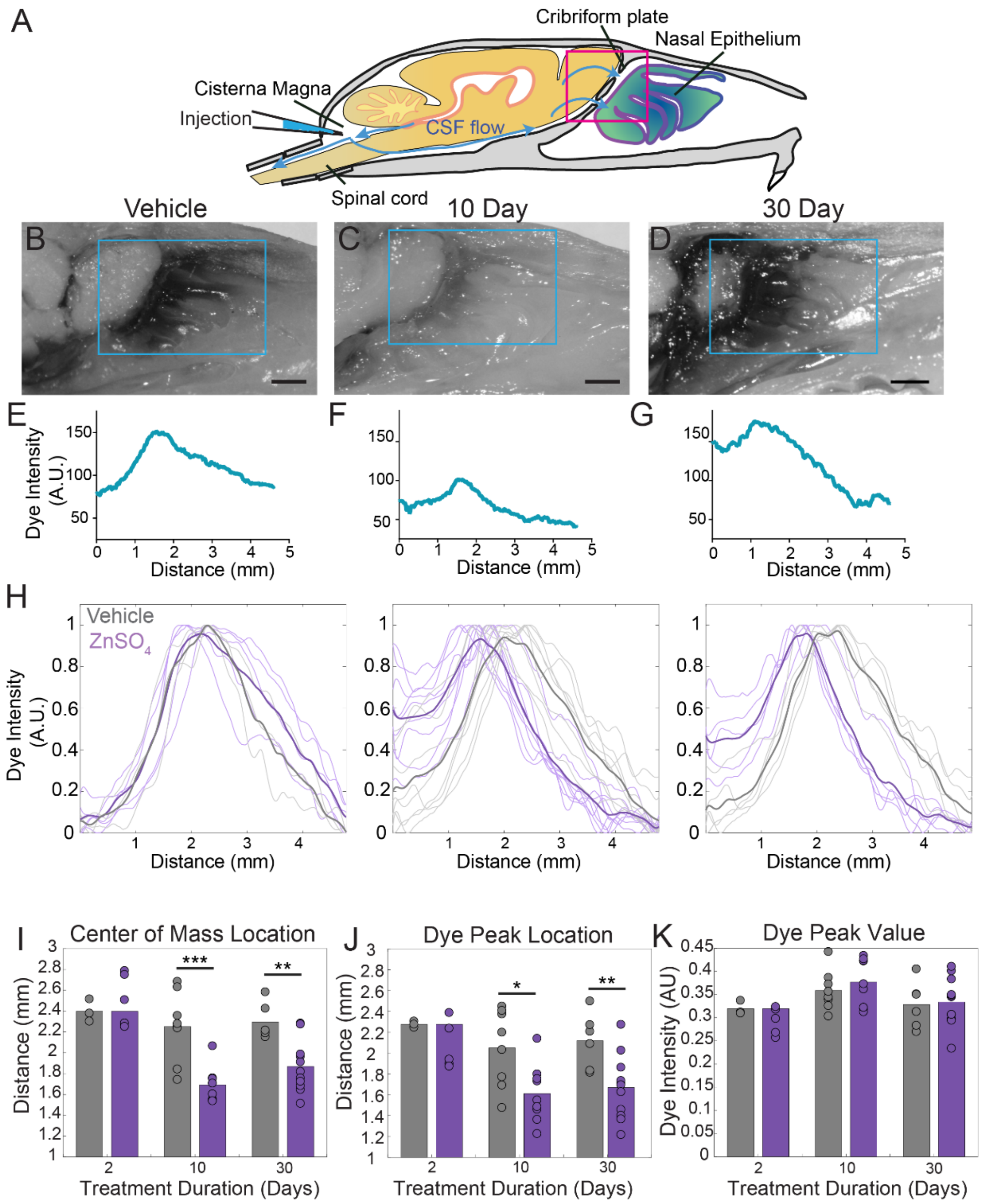

Figure 7: $ZnSO_4$ treatment decreases CSF outflow through the cribriform plate ipsilateral to treatment. A) Sagittal view schematic depicting direction of CSF flow and location of a cisterna magna injection of Evans blue. **B-D)** Sagittal view of decalcified and cut skull for imaging after Evans blue injection, area indicated by pink box in **(A).** ROI indicated by blue box. Scale bar 1mm. **B)** Vehicle control. **C)** 10 day $ZnSO_4$ treated. **D)** 30 day $ZnSO_4$ treated **E-G)** Plot of the intensity of the Evans blue dye as a function rostral-caudal distance. **E)** Vehicle control, ROI of area measured indicated by blue box in **(B)**. **F)** 10 day $ZnSO_4$ treated, ROI of area measured indicated by blue box in **(C). G)** 30 day $ZnSO_4$ treated, ROI of area measured indicated by blue box in **(D). H)** Comparison of all dye curves of all vehicle (gray) and $ZnSO_4$ treated (purple) groups for each treatment duration: 2 day, n= 3 vehicle and n = 5 treated. 10 day, n = 5 for each group. 30 day, n = 6 vehicle and n = 11 for treated. Means plotted as bold lines. **I-K)** Mean is plotted as height of bar. Circles represent individual animals. **I)** Mean of the center of mass location of the dye curve plotted for vehicle and zinc treated animals after 2 (t(6) = 0.7489, p = 0.4822, n = 3

vehicle and n = 5 treated, post-hoc ttest2) , 10 (t(15) = -4.4921, p = 0.0004, n = 5 for each group, post-hoc ttest2) , and 30 ((t(15) = -3.7539, p = 0.0019, n = 6 vehicle and n = 11 for treated, post-hoc ttest2) days of treatment. **J)** Mean dye peak location plotted for vehicle and $ZnSO_4$ treated animals after 2 (t(6) = -1.5082, p = 0.1822, n = 3 vehicle and n = 5 treated, post-hoc ttest2), 10 (t(15) = -2.8064, p = 0.0133, n = 5 for each group, post-hoc ttest2), and 30 (t(15) = -3.0014, p = 0.0089, n = 6 vehicle and n = 11 for treated, post-hoc ttest2) days of treatment. **K)** Maximum dye peak value plotted for vehicle and $ZnSO_4$ treated animals after 2 (t(6) = -1.4187, p = 0.2058, n = 3 vehicle and n = 5 treated, post-hoc ttest2), 10 (t(15) = 0.7982, p = 0.4372, n = 5 for each group, post-hoc ttest2), and 30 (t(15) = 0.2052, p = 0.8402, n = 6 vehicle and n = 11 for treated, post-hoc ttest2) days of treatment. *p≤0.05 **p≤0.01. ***p≤0.001

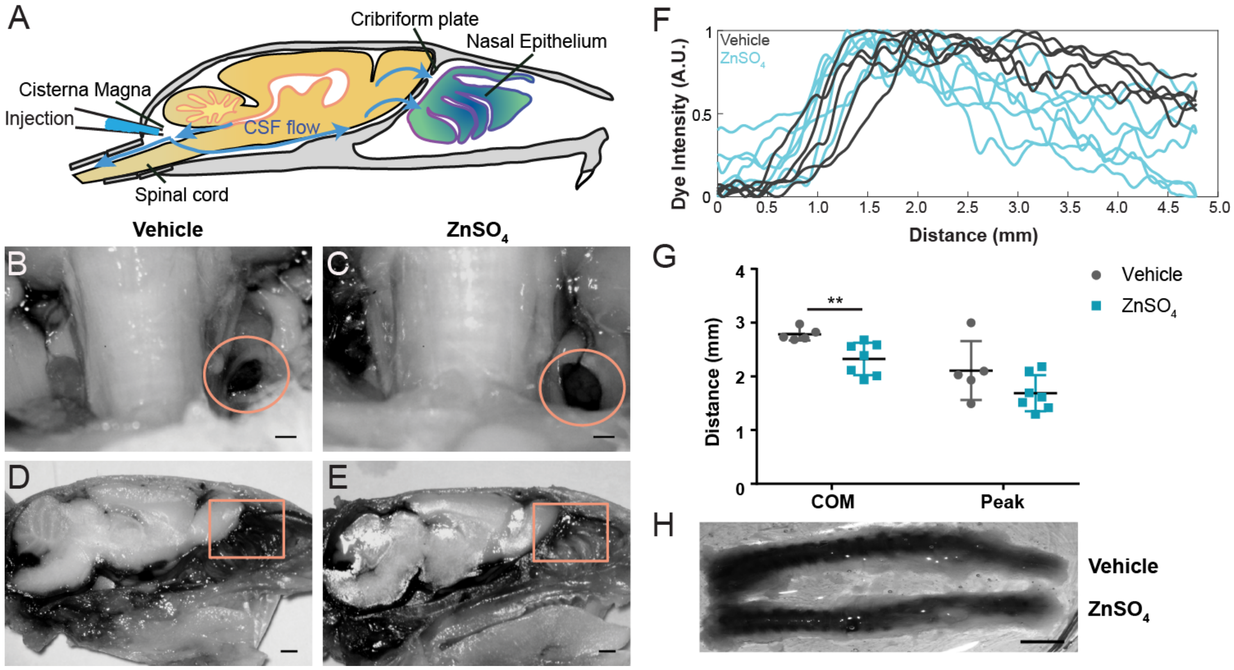

Figure 8: Longer-duration dye injections show $ZnSO_4$ treatment blocks CSF flow across the cribriform plate **A**) Sagittal view of the skull depicting direction of CSF flow and location of cisterna magna injection of EB. **B-C)** Localization of EB dye in the deep cervical lymph nodes (orange circles) after a cisterna magna EB injection**.** Scale bar 500 μm. **B)** Vehicle control. **C)** 30 day $ZnSO_4$ treated. **D-E)** Sagittal view of decalcified and cut skull of the ipsilateral side for imaging after EB injection in the cisterna magna**.** ROI indicated by orange box. Scale bar 1mm. **D)** Vehicle control. **E)** 30 day $ZnSO_4$ treated. **F)** Plot of the intensity of the Evans blue dye as a function rostral-caudal distance for vehicle (gray) and $ZnSO_4$ treated (blue) groups for 30 day treatment duration**.** ROI indicated by orange box in **(D-E)**. **G)** Mean of the center of mass (t(10) = -3.2015, p = 0.0095, n = 5 vehicle and n = 7 treated, post-hoc ttest2) and dye peak (t(10) = -1.6604, p = 0.1278, n = 5 vehicle and n = 7 treated, post-hoc ttest2) location of the curve plotted for vehicle and $ZnSO_4$ treated animals for 30 day treatment duration. **H)** Vehicle (top) and 30 day $ZnSO_4$ treated (bottom) decalcified and SeeDB cleared spinal columns after cisterna magna EB injection. Scale bar 500 mm.

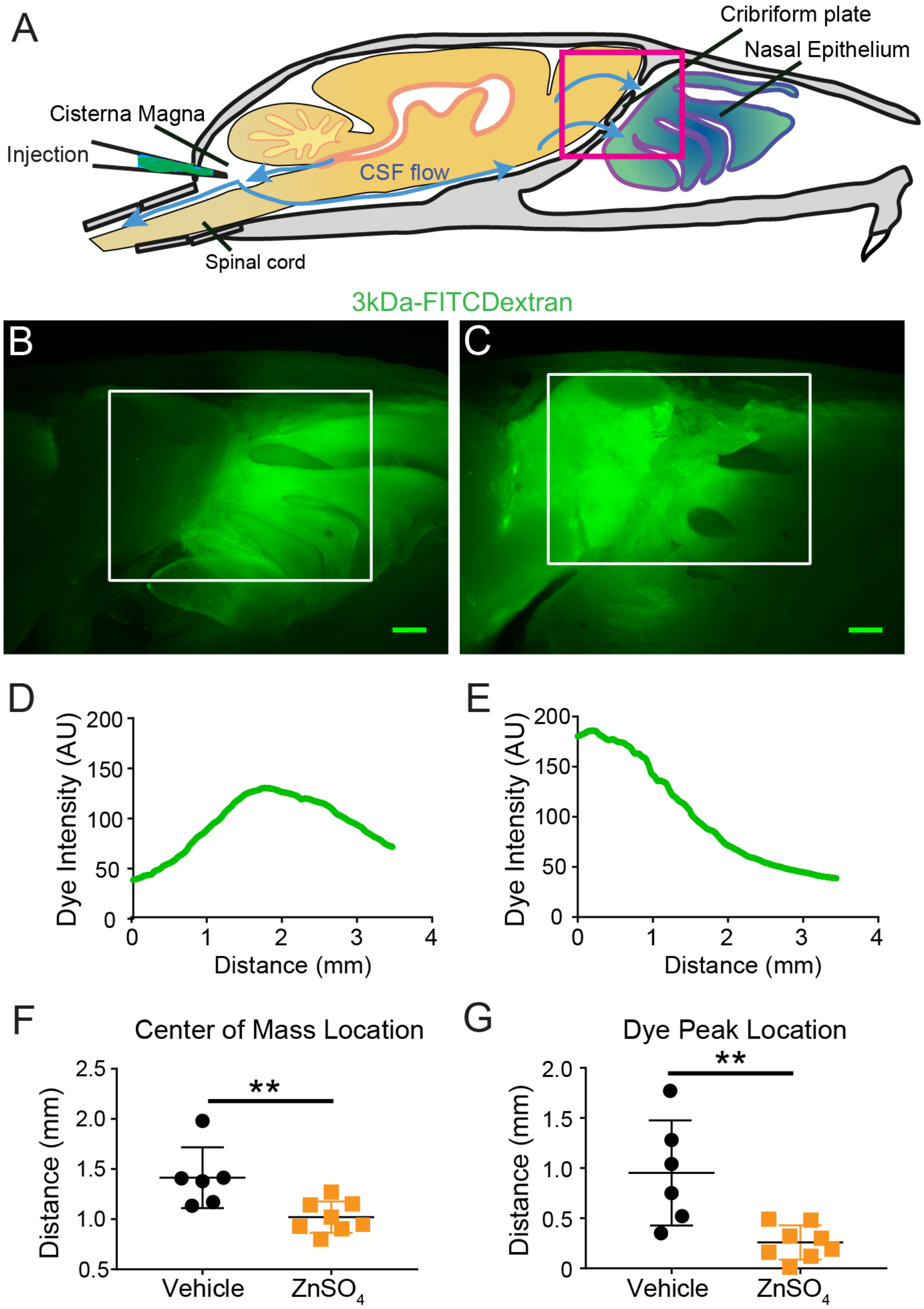

Figure 9: Visualization of effects of intranasal $ZnSO_4$ treatment on CSF flow with 3kDa-FITC Dextran. A) Schematic of a sagittal view of the skull, depicting direction of CSF flow and location of cisterna magna injection of 3kDa-FITCDextran. **B-C)** Sagittal view of decalcified and cut skull for imaging after FITC-dextran injection, area indicated by pink box in **(A).** Scale bar 500 µm. **B)** Vehicle control. **C)** 10 day $ZnSO_4$ treated. **D-E)** Plot of the intensity of the 3kDa-FITC Dextran dye as a function of rostral-caudal distance. **D)** Vehicle control, ROI of area measured indicated by white box in **(B)**. **E)** 10 day $ZnSO_4$ treated, ROI of area measured indicated by white box in **(C). F-G)** Mean ± standard deviation plotted. Circles and squares represent means of individual animals. **F)** Comparison of the center of mass location of the dye peak between the vehicle (black) and $ZnSO_4$ (orange) treated groups (t(12) = -3.1805, p = 0.0079, n = 6 vehicle and n = 8 treated, post-hoc ttest2). **G)** Comparison of the location of the dye peak between the vehicle (black) and $ZnSO_4$ (orange) treated groups (t(12) = -3.5384, p = 0.0041, n = 6 vehicle and n = 8 treated, post-hoc ttest2). $^{**}p \leq 0.01$. Note that the time between cisterna magna injection and

sacrifice was different in the FITC-dextran and EB injections (35 vs. 20 minutes respectively) due to the different molecular weights of the dyes.

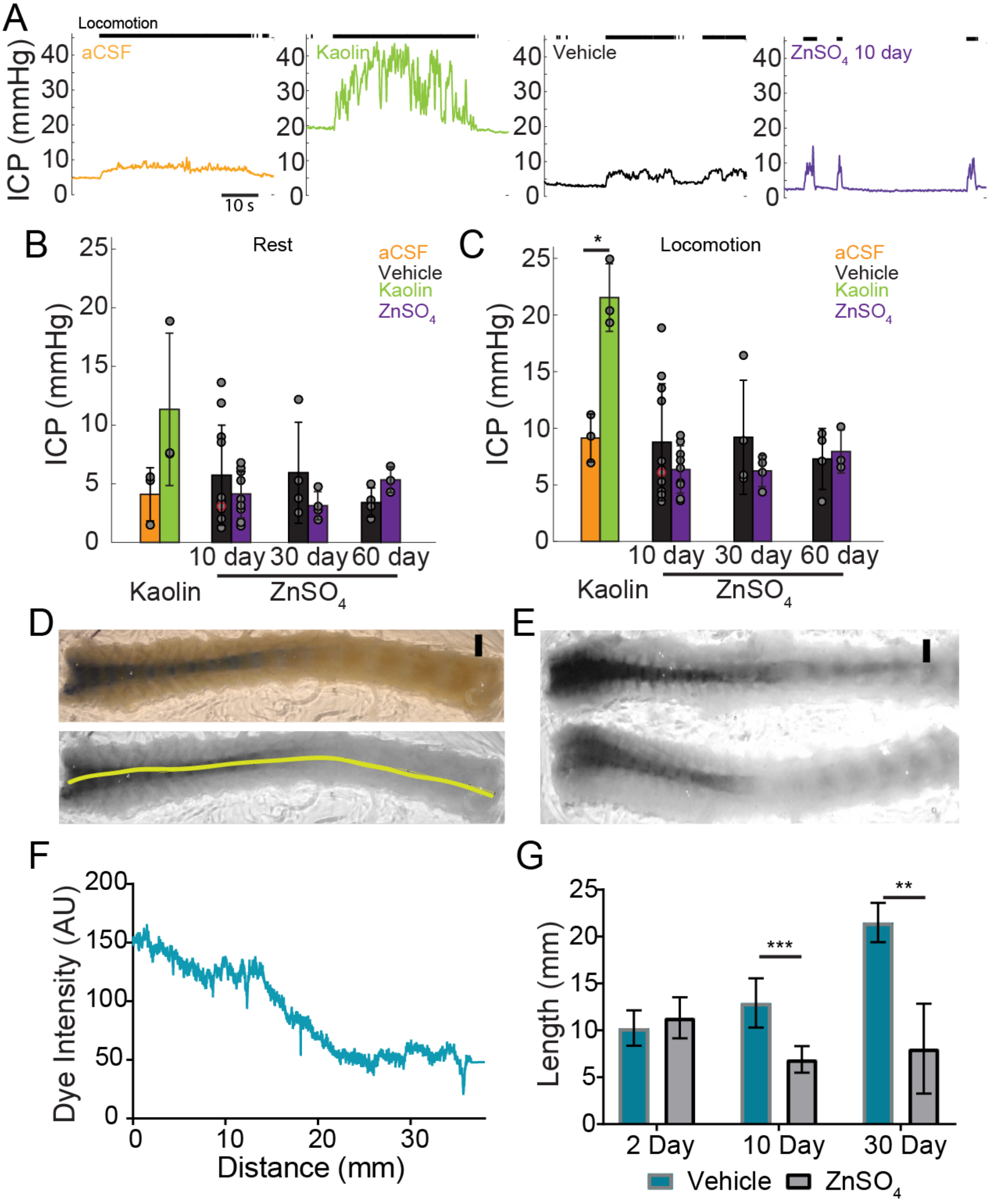

Figure 10: Intranasal $ZnSO_4$ treatment does not affect ICP but decreases CSF movement down the spinal column. A) Left panel, example trace showing intracranial pressure (ICP) change during a locomotion bout in an animal that has been injected with aCSF in the cisterna magna. The ICP becomes elevated slightly over baseline when the animal moves, consistent with previous results[72]. The tick marks in the upper panel indicates locomotion events, defined as times where the treadmill acceleration exceeds a thereshold[75]. Subsequent panels show ICP

change during locomotion in animals injected with Kaolin, vehicle control, or $ZnSO_4$ treatment, respectively. **B)** Mean of each group of ICP during rest after kaolin injection (Kaolin) and 10, 30, and 60 days after treatment ($ZnSO_4$). The orange shaded circle indicates the same animal showing in **(A)**. **C)** Same as **(B)** but for ICP during locomotion. Comparison of ICP during locomotion for aCSF and kaolin injected mice (t(4) = 5.88, p = 0.0042, n=3 for each group, ttest2). **B-C)** No statistically significant differences were observed between $ZnSO_4$-treated and control animal at rest or during locomotion for all treatment durations (Mixed model ANOVA, F(1,33) = 3.01, p = 0.0921, PROC MIXED, SAS 9.4). Mean ± standard deviation plotted. Circles represent individual animals. **D)** Top panel: A decalcified and SeeDB-cleared spinal column after a cisterna magna EB injection. Bottom panel: Red channel only displaying the trace (yellow line) used for quantifying pixel intensity. Scale bar 2mm. **E)** Vehicle (top) and 10 day $ZnSO_4$ treated (bottom) decalcified and SeeDB cleared spinal columns after cisterna magna EB injection. **F)** Trace obtained and graphed to display dye intensity of EB along the spinal column (distance) quantified after cisterna magna injections. **G)** Comparisons of the distance of dye movement along the spinal column after an EB cisterna magna injection in mice intranasally treated with vehicle or $ZnSO_4$, 2 (t(5) = 0.6921, p = 0.5197, n = 3 vehicle and n = 4 treated, ttest2), 10 (t(12) = 5.069, p = 0.00028, n = 8 vehicle and n = 6 treated, ttest2), and 30 days (t(9) = 4.571, p = 0.00134, n = 3 vehicle and n = 8 treated, ttest2), after treatment. Mean ± standard deviation plotted. $*p \leq 0.05$ $**p \leq 0.01$ $***p \leq 0.001$.